Tracing ancient hydrogeological fracture network age and compartmentalisation using noble gases

Authors: [1,2]Oliver Warr *(corresponding author)*, [2]Barbara Sherwood Lollar, [3]Jonathan Fellowes, [2]Chelsea N. Sutcliffe, [2]Jill M. McDermott, [3]Greg Holland, [1]Jennifer C. Mabry & [1]Christopher J. Ballentine

[1] Department of Earth Sciences, University of Oxford, South Parks Road, Oxford, OX1 3AN, United Kingdom. Email: oliver.warr@utoronto.ca, phone: +1 416 978 3022

[2] Department of Earth Sciences, University of Toronto, Toronto, Ontario, Canada.

[3] School of Earth, Atmospheric and Environmental Sciences, Williamson Building, University of Manchester, Manchester, M13 9PL, United Kingdom.

Abstract

We show that fluid volumes residing within the Precambrian crystalline basement account for ca 30 % of the total groundwater inventory of the Earth (> 30 million km^3). The residence times and scientific importance of this groundwater are only now receiving attention with ancient fracture fluids identified in Canada and South Africa showing: 1. microbial life which has existed in isolation for millions of years; 2. significant hydrogen and hydrocarbon production via water-rock reactions; and 3. preserving noble gas components from the early atmosphere. Noble gas (He, Ne, Ar, Kr, Xe) abundance and isotopic compositions provide the primary evidence for fluid mean residence time (MRT). Here we extend the noble gas data from the Kidd Creek Mine in Timmins Ontario Canada, a volcanogenic massive sulfide (VMS) deposit formed at 2.7 Ga, in which fracture fluids with MRTs of 1.1-1.7 Ga were identified at 2.4km depth (Holland et al., 2013); to fracture fluids at 2.9km depth. We compare here the Kidd Creek Mine study with noble gas compositions determined in fracture fluids taken from two mines (Mine 1 & Mine 2) at 1.7 and 1.4 km depth below surface in the Sudbury Basin formed by a meteorite impact at 1.849 Ga.

The 2.9 km samples at Kidd Creek Mine show the highest radiogenic isotopic ratios observed to date in free fluids (e.g. $^{21}Ne/^{22}Ne$ = 0.6 and $^{40}Ar/^{36}Ar$ = 102,000) and have MRTs of 1.0 to 2.2 Ga. In contrast, resampled 2.4 km fluids indicated a less ancient MRT (0.2-0.6 Ga) compared with the previous study (1.1-1.7 Ga). This is consistent with a change in the age distribution of fluids feeding the fractures as they drain, with a decreasing proportion of the most ancient end-member fluids. $^{129}Xe/^{136}Xe$ ratios for these fluids confirm that boreholes at 2.4 km versus 2.9 km are sourced from hydrogeologically distinct systems. In contrast, results for the Sudbury mines

have MRTs of 0.2-0.6 and 0.2-0.9 Ga for Mines 1 and 2 respectively. While still old compared to almost all groundwaters reported in the literature to date, these younger residence times compared to Kidd Creek Mine are consistent with significant fracturing created by the impact event, facilitating more hydrogeologic connection and mixing of fluids in the basin. In all samples from both Kidd Creek Mine and Sudbury, a $^{124\text{-}128}$Xe excess is identified over modern air values. This is attributed to an early atmospheric xenon component, previously identified at Kidd Creek Mine but which has to date not been observed in fluids with a residence time as recent as 0.2-0.6 Ga. The temporal and spatial sampling at Kidd Creek Mine is also used to verify our proposed conceptual model which provides key constraints regarding distribution, volumes and residence times of fracture fluids on the smaller, regional, scale.

1 Introduction

Brines rich in helium, hydrogen, methane and nitrogen within Precambrian crustal rocks have been shown to provide habitable environments for subsurface microbial life (Chivian et al., 2008; Lin et al., 2006; Lau et al., 2016; Magnabosco et al., 2016). The global significance of such ancient rocks for sustaining subsurface life has recently been demonstrated through the identification of water-rock reactions producing electron donors (e.g. hydrogen; Sherwood Lollar et al., 2014) and electron acceptors (e.g. dissolved sulfate; Li at al., 2016). Recent studies have also shown there is significant methanogenesis in these fracture waters, via both microbial methanogenesis, and abiotic water-rock interactions such as Fischer-Tropsch synthesis (Sherwood Lollar et al., 2002; Sherwood Lollar et al., 2006; Kietäväinen and Purkamo, 2015). The significance of these Precambrian crustal systems in global hydrogen production and deep

carbon cycles has only recently been investigated (Sherwood Lollar and Ballentine, 2009; Etiope and Sherwood Lollar, 2013; Sherwood Lollar et al., 2014). Given the long residence times of some of these fracture fluids (> 1 Ga Holland et al., 2013; Lippmann-Pipke et al., 2011), and the discovery of ancient components of other elements (e.g. Archean atmospheric derived xenon Holland et al., 2013; mass independent sulfur isotope signatures; Li et al., 2016), it is reasonable to expect these types of system may have affected global cycles over geological and planetary timescales. The exploration for microbial life (Pedersen et al., 2005; Lin et al., 2006; Chivian et al., 2008), in these ancient terrestrial rocks focuses on developing an understanding of the distribution of biomass and biodiversity, which when coupled with a quantitative estimate of the mean residence times of the fluids within which life is found may provide insights into the evolution and distribution of microbial life over the course of the Earth's history (Sherwood Lollar and Ballentine, 2009; Onstott et al., 2010; Kietäväinen and Purkamo, 2015).

To advance this new area of research, the distribution of residence times of the fluids within different regions of the >70 % of the continental lithosphere that is Precambrian in age is required. This information will address the compartmentalization of the deep hydrogeosphere - the degree of hydrogeological connection between different fracture fluid systems, and/or their degree of isolation from each other and the surface hydrosphere. The unique properties of noble gases can be applied to constrain these variables (Holland et al., 2013; Lippmann-Pipke et al., 2011; Sherwood Lollar and Ballentine, 2009).

The Kidd Creek Mine deposit in the Superior Province of the Canadian Shield is the site where previous noble gas analysis of fluid samples rich in helium, hydrogen, methane and nitrogen collected at 2.4 km depth from a copper-zinc mine in Timmins, Ontario, identified the oldest isolated fracture fluids, with a mean residence time range of 1.1 – 1.7 Ga (Holland et al., 2013).

This age was based on a radiogenic excess of ^{4}He, ^{21}Ne, ^{40}Ar and ^{136}Xe, a preserved early atmospheric $^{124\text{-}128}Xe$ signal and a sedimentary-derived ^{129}Xe excess (assumed to be from a localised sedimentary source). This study documented fluids with the longest mean residence times ever observed in the crust to date, and showed that fracture fluids in these Precambrian systems could be isolated on planetary timescales. Since this study the Kidd Creek Mine has been expanded to an even deeper level (2.9 km). The three main objectives of this study were 1. to resample the fracture fluids identified by Holland et al. (2013) in to order to test the hypothesis that in the 44 months since the previous study the mean residence time would decrease due to draining of fractures (See Section 5.2 & Figure 7); 2. to sample the new deeper levels of the Kidd Creek Mine site to understand the distribution of ancient fluids; and 3. to compare and contrast the fluids from Kidd Creek Mine to those of two new sites in the Sudbury Basin. The two Sudbury mines are situated in 2.6-2.7 Ga Archean bedrock underlying the Sudbury Igneous Complex, a 1.849 Ga formation produced by a bolide impact (Krogh et al., 1984; Card, 1994; Davis, 2008). The impact produced major fracturing of the bedrock and hence likely opened significantly more lines of structural weakness along which fluid movement and mixing could occur compared to the relatively less disturbed geologic setting at Kidd Creek Mine.

2 Geological Background

2.1 Geology of the Superior Province of the Canadian Shield - Kidd Creek Mine, near Timmins, Ontario, Canada

Kidd Creek Mine, Timmins, Ontario **(**Figure 1) is situated 24 km north of the town of Timmins, within a stratiform Volcanogenic Massive Sulphide (VMS) deposit of 2.7 Ga age (Thurston et al., 2008). This deposit lies within the Kidd-Munro assemblage of the Southern Volcanic Zone of the Abitibi greenstone belt of the Superior Province of the Canadian Shield (Bleeker and Parrish, 1996). The Kidd-Munro assemblage itself consists of a series of steeply dipping interlayered felsic, mafic, ultramafic and metasedimentary deposits. One of the primary economic resources, the stringer ore, is predominantly associated with the upper felsic region and formed as a result of silica and metal-rich hydrothermal fluid circulation below the seafloor. Above the stringer ore deposits lie banded and massive sulphide ores. These are considered to have been initially deposited as inorganic precipitates formed where hydrothermal solutions rich in metals entered the seawater. Intermittent argillite to chert carbonaceous horizons within the assemblage represent periods of volcanic quiescence during which proximal seafloor sediments accumulated. Following deposition of the Kidd-Munro assemblage, the entire formation was metamorphosed to greenschist facies during the last major regional metamorphic event at 2.67-2.69 Ga. The last known episode of metasomatism occurred at 2.64 Ga (Davis et al., 1994; Bleeker and Parrish, 1996; Thurston et al., 2008; Berger et al., 2011).

Kidd Creek Mine was opened in 1964 as an open pit. Since then it has been developed vertically to a depth of 2.9 km. In this facility, mining involves lateral coring via multiple boreholes at each level as described in detail in Li et al. (2016). Exploration boreholes frequently intersect pockets of fracture fluids trapped within the host rock. Once pierced, fluids from these pockets have been observed to flow over prolonged time periods, in some cases > 7 years since first discovered by

130 our team. Gas samples taken from these fracture fluids were analyzed for their noble gas content,
131 following the methods of Ward et al. (2004) and Holland et al. (2013).
132
133 **2.2 Geology of the Sudbury Basin and underlying Archean basement, near Sudbury,**
134 **Ontario, Canada**
135 The Sudbury Basin is located approximately 300 km south-east of Kidd Creek Mine (Figure 1).
136 The Sudbury Impact Complex (SIC) formed at 1.849 Ga by an estimated 10-15 km diameter
137 meteorite impacting the Archean basement (consisting of carbonaceous shale, metavolcanic and
138 metasedimentary rocks, gneisses & related intrusive rocks, primarily 2.6-2.7 Ga in age, Card,
139 1994; Meldrum et al., 1997; Davis, 2008). The resulting impact-induced melting and
140 differentiation formed noritic to gabbroic cumulates overlain by residual granophyres (Pattison,
141 2009). Magmatic sulphide deposits at the base of the SIC contact, along with associated dykes
142 and breccia in the footwall together, form one of the world's largest nickel, copper, platinum,
143 and palladium economic resources exploited by multiple mining operations (Long, 2009). The
144 region has been deformed by three main major orogenic events: the Penokean (1.89-1.830 Ga);
145 the Mazatzal (1.7-1.6 Ga) and the Grenville (1.4-1.0 Ga). Most recently the North-Eastern
146 section of the Sudbury structure was deformed by yet another impactor forming Lake Wanapitei
147 (37 Ma). The basin and underlying Archean basement rocks have been heavily faulted and
148 folded and metamorphosed up to granulite facies between 2.6-2.7 Ga and more recently
149 amphibolite facies at 1.9-1.8 Ga (James and Golightly, 2009 and references therein).
150
151 Both Sudbury mines sampled in this study are located in the footwall of the basin, hosted in 2.6-
152 2.7 Ga Levack Gneiss Archean basement. The first mine (Mine 1) is at 1.7 km depth and the

second mine (Mine 2) is at 1.4 km depth. Both Mine 1 and Mine 2 are nickel-copper mines and are located in the northeast and northwest region of the Sudbury Impact Complex, approximately 25 & 33 km from the City of Sudbury respectively. Mine 1 has been in operation since 2006 and Mine 2 since 1984. As with Kidd Creek Mine, isolated pockets of fracture fluids within the host rock were accessed via lateral boreholes.

2.3 Sample Collection

All samples were collected at the borehole collars from which fluids (and dissolved gases) were naturally flowing (Table 1) (see Holland et al., 2013 and Li et al., 216 for detailed description). Briefly, as in previous studies, an inflatable packer was inserted into the borehole opening to prevent any atmospheric contamination (e.g. Holland et al., 2013; Sherwood Lollar et al., 2002; Ward et al., 2004). Fluids from each borehole were allowed to separate into gas and water phases by flowing through a gas stripper. Gas samples from fracture fluids were collected in refrigeration-grade, internally polished, 3/8" diameter copper tubes used routinely in noble gas studies. Prior to sample collection, any air contamination was flushed out of the sampling apparatus and copper tubes by flowing borehole fluids through the equipment for a minimum of 20 minutes (as a function of the flowrates and volume of the sampling apparatus). Once flushing to remove air contamination was complete and a representative sample of the fracture fluids established, the copper tubes were cold-welded shut using a hydraulic crimping device. Samples were collected from Kidd Creek Mine at 2.4 km and 2.9 km depth and from Sudbury Mines 1 and 2 at 1.7 and 1.4 km depth respectively. As noted, the sample at 2.4 km were samples from

176 the same boreholes reported by Holland et al. (2013). For the samples at 2.9 km, due to mine
177 operations, no water samples could be collected (standing water only in the boreholes with no
178 artesian flow in this case), but gas samples were collected using the same methodology as above.
179
180
181 **3 Sample Analysis**
182 Samples were analyzed using a combined dual mass spectrometer and purification system in the
183 Noble Laboratory at the Department of Earth Sciences, University of Oxford (Barry et al., 2016).
184 Samples were mounted on to the purification system by clamping the copper tubes adjacent to
185 the cold weld using standard clamping procedures, removing the cold weld, and connecting to
186 the line using a stainless-steel tube fitting to form a metal on metal seal. Ultra-High Vacuum
187 (UHV) was reached using a combination of roughing and turbo pumps. Prior to sample analysis
188 the integrity of the metal seal for each mounted sample was verified via standard helium leak
189 testing (e.g. Warr et al., 2015).
190
191 **3.1 Separation of noble gases**
192 Given the extremely radiogenic nature of these samples, efficient separation of helium from neon
193 and argon from krypton and xenon was essential. This was achieved through a process of repeat
194 cycling of the respective traps, and static or dynamic pumping for He/Ne and Ar/Kr and Ar/Xe
195 respectively. In all cases separation with no loss or fractionation was verified using procedural
196 air calibrations which were analyzed using the same protocols. Removal of helium was
197 confirmed via the Helix SFT prior to neon release, and argon separation was verified via
198 measurement post-Kr and Xe analysis. In both cases, residual helium and argon analyzed during

199 the neon and the krypton/xenon analyses respectively were estimated to be < 0.005 % of their
200 original intensities and have no pressure effect on the neon or krypton/xenon measurements.

201

202 **3.2 Analytical procedure**

203 Initially samples and procedural standards were expanded to a known volume fitted with a 1000
204 Torr Baratron, and the pressure and temperature of the sample was recorded. Next the sample
205 was exposed to approximately 30 g of activated titanium sponge held at 1223 K (950 °C) to
206 chemically remove the majority of the active gases. After 30 minutes the sponge was allowed to
207 cool for a further 30 minutes to allow removal of H_2 (Stout and Gibbons, 1955). The sample was
208 further purified for an additional 15 minutes using a combination of a hot (SAES GP-50) and
209 cold (SAES NP-10) getters. The cleaned gas was then passed through a series of helium-cooled
210 calibrated cryogenic traps to 1. remove water vapour (stainless steel, 180 K) 2. trap argon,
211 krypton and xenon (stainless steel, 33 K) and 3. trap helium and neon (charcoal, 15 K). Each
212 trapping stage lasted 15 minutes (Barry et al., 2016).

213

214 For helium analysis, the charcoal trap was heated to 31 K for 15 minutes, split using known
215 volume expansions and then measured using a HELIX SFT. Peak centres were defined manually
216 and ^{3}He and ^{4}He were measured simultaneously on an electron multiplier and on a Faraday
217 respectively.

218 In order to measure neon, it was necessary to first remove any residual helium from the system.
219 This was efficiently achieved by developing a technique for these highly radiogenic samples
220 which cycled the charcoal trap to 50 K for 15 minutes then back down to 31 K for a further 15

minutes. This allowed any potential trace helium (<< 1 %) still adsorbed to the charcoal as well as residual helium in the headspace, to be released while trapping all neon. The gas was then expanded to the manifold and pumped, during which the charcoal trap was isolated. This non-dynamic heating, cooling and pumping process was repeated two further times.

Next, following the methods of Barry et al. (2016), the charcoal trap was heated to 90 K for 15 minutes to release all neon and a known volume was inlet into the ARGUS VI for measurement. Each analysis consisted of peak-jumping in which ^{20}Ne and ^{22}Ne were measured on Faraday cups and ^{21}Ne was measured on a multiplier. Additionally, during each cycle, ^{40}Ar and CO_2 were measured to allow correction for $^{40}Ar^{++}$ and CO_2^{++} interference peaks. Following the measurement, the charcoal trap was heated to 300 K, opened to the vacuum pump to remove any remaining sample, and then isolated from the line.

For argon measurements, the stainless-steel trap was heated to 200 K for 15 minutes to release all noble gases; from which a small aliquot is taken. Once this aliquot was taken the trap was cooled back down to 52 K to re-trap the heavy noble gases. The aliquot was expanded and diluted using calibrated volumes to reduce the ^{40}Ar to measurable levels. The gas was then inlet to the ARGUS VI which measured ^{36}Ar and ^{38}Ar on an electron multiplier and ^{40}Ar on a Faraday cup via peak-jumping.

In order to measure krypton and xenon it was necessary to isolate and remove the residual argon. This was accomplished through a series of trap cycling and pumping steps specifically developed for these highly radiogenic samples. Here the stainless-steel trap was cycled from 52 K to 70 K, to release Ar, then back down to 52 K, waiting 15 minutes to allow full re-trapping of Kr and Xe then 5 minutes dynamic pumping to remove the argon. After 5 cycles the stainless-steel trap was

heated to 200 K to ensure release of all noble gases. The sample was then inlet into the ARGUS where all krypton and xenon isotopes were measured in one analysis using peak jumping. During this measurement ^{78}Kr, ^{124}Xe and ^{126}Xe were measured on the electron multiplier and the remaining isotopes were measured using Faraday cups.

3.3 Standards and line blanks

At the beginning of the sample suite a full procedural air standard was run from an air cylinder which was collected 24.11.14 in University Parks, Oxford, UK. This standard was collected under known environmental conditions (5 °C, 89 % humidity and 1027 mBar pressure) as per standard procedures for noble gas analysis (Warr et al., 2015; Barry et al., 2016)). For comparison between sample and standard the pressure was measured using the 1000 Torr Baratron over the same volume used for sample inlet. Analysis of the air standard followed the same procedure as the samples. Additionally, a full procedural system blank using the sample protocol was also run mid-way through the sample suite to provide a measure of background for subtraction. To factor in any day-to day changes in mass spectrometer sensitivity, and confirm reproducibility, a separate and fully automated standard was analysed, usually overnight, in between samples, procedural blanks and procedural air standards.

All analytical errors were propagated using the standard addition in quadrature method (e.g. Warr et al., 2015). Where averages are used (e.g. for each mine level Tables 2-5) the error is taken as the standard deviation of individual data points, which is always comparable to, or greater than, analytical uncertainty for the individual data points.

4 Results

266

267 All ratios and concentrations of representative isotopes are presented respectively in Tables 2-6.

268

269 **4.1 Concentrations of noble gases**

270 In geological systems where water-rock reactions have been shown to produce significant
271 concentrations of reactive gases such as H_2, methane, and other hydrocarbon gases (Sherwood
272 Lollar et al., 2002; Sherwood Lollar et al., 2014), absolute concentrations of conservative noble
273 gases per cm^3 of gas (Table 2) are of limited utility. This is because noble gas concentrations
274 within the gas phase may have been affected by both *in situ* H_2 and CH_4 production and addition,
275 and loss of reactive gases through other sinks in the subsurface (e.g. water rock interactions, or
276 microbial uptake). As a result of these processes noble gas concentrations within the gas phase
277 can become passively enriched or diluted. However, initial concentrations within the fracture
278 fluids can be reconstructed using non-radiogenic isotopes coupled with measured isotopic ratios
279 after the method of Holland et al., 2013. This method assumes that the ^{36}Ar in the sampled gas is
280 entirely derived from water that equilibrated with the atmosphere. Here we take seawater at 10
281 $^{\circ}C$ as our initial ^{36}Ar composition (Kipfer et al., 2002) following the arguments of Holland et al
282 (2013). The ^{36}Ar concentration measured in the gas phase then allows calculation of the volume
283 of water required to completely degas to provide that amount of ^{36}Ar (e.g. Ballentine et al., 1991;
284 Ballentine et al., 2002), thereby allowing calculation of the total gas/water ratio for the
285 concentration of each individual species within this nominal associated water mass. Selected
286 radiogenic and non-radiogenic noble gas isotopes are given as concentrations within the nominal
287 associated water mass and presented as concentrations in cm^3 per cm^3 of fracture fluid at STP

conditions (Table 3, 4). Values for all isotopes are additionally provided in Appendix A. These are the concentrations which are discussed in the remainder of this section.

4.2 Concentrations of air-saturated components

Through normalising non-radiogenic isotopes (Table 3) to a single isotope (^{36}Ar) it is possible to compare elemental ratios in samples with elemental ratios in air-saturated seawater at 10 °C, in order to identify any elemental fractionation within each system and assess how reasonable the inferred starting composition is. This is presented in Figure 2.

Partial degassing of fluids with an initial ASW concentration via open Rayleigh degassing would result in a gas composition enriched in ^{20}Ne and depleted in ^{84}Kr and ^{130}Xe relative to ^{36}Ar. This observation does not match observed ratios for the resampled boreholes from 2.4 km at Kidd Creek Mine, nor samples from Mines 1 & 2. Hence no major fractionation related to degassing is inferred for ^{20}Ne, ^{84}Kr or ^{130}Xe for these samples. This lack of observable solubility-dependent loss/gain outside of uncertainty suggests that near complete degassing of the original fluid phase has occurred. Hence the data for these samples do not require any post-processing to account for only partial degassing of the fracture fluid. Small deviations from expected elemental ratios are likely due to the large current uncertainty in initial temperature and salinity from the assumed starting conditions (seawater at 10 °C), both of which can have an effect on noble gas solubility (Crovetto et al., 1982; Smith, 1985; Smith and Kennedy, 1983).

In contrast, in the case of Kidd Creek Mine samples from 2.9 km depth, there is evidence for Rayleigh fractionation on a localised borehole scale (Appendix C) which has created an enrichment of ^{20}Ne coupled with a deficit of ^{84}Kr and ^{130}Xe relative to ^{36}Ar. With ^{36}Ar values

depleted by 17 % from the assumed starting conditions. A correction for this has been applied to each noble gas (30.6 %, 29.6 %, 17.0 %, 11.4 %, & 8.4 % for helium – xenon respectively) based on their respective solubilities and the recalculated radiogenic excesses for each noble gas are presented in Table 7. These are the values referred to when discussing radiogenic concentrations and the residence time calculations in Section 4.10. A comprehensive discussion and quantification of the degassing is provided in Appendix C.

4.3 Helium

In all samples in this study, the $^{3}He/^{4}He$ ratios are consistent with typical crustal radiogenic production rates estimated for crystalline rock globally (Ballentine and Burnard, 2002). Consistent with previous work in these tectonically quiescent environments, no mantle component is observed (Sherwood Lollar et al., 1993; Lippmann-Pipke et al., 2011; Holland et al., 2013). The $^{3}He/^{4}He$ ratios for all samples are given in Table 5. As per convention these ratios are given in R_A where 1 R_A is the atmospheric ratio (1.4×10^{-6}). All helium ratios are highly radiogenic (< 0.026 Ra). This is reinforced by the absolute average concentrations of ^{4}He per cm^3 of fracture fluid which in Kidd Creek Mine range between 0.08 (at 2.4 km) and 0.36 cm^3 ^{4}He per cm^3 of fracture fluid (at 2.9 km) and 0.06 and 0.03 cm^3 ^{4}He per cm^3 of fracture fluid in Mine 1 (at 1.7 km) and Mine 2 (at 1.4 km) respectively for the Sudbury system. These concentrations are at least six orders of magnitude greater than the initial ASW concentration (Kipfer et al., 2002). Consequently, any air-derived component present is negligible and no corrections need to be applied.

332 **4.4 Neon**

333 For all samples, isotopic ratios of $^{21}Ne/^{20}Ne$ and $^{22}Ne/^{20}Ne$ are greater than ASW due to a
334 resolvable excess of radiogenic ^{21}Ne and ^{22}Ne. In the resampled fracture fluids from 2.4 km at
335 Kidd Creek Mine, average ^{21}Ne excesses are 3.2 $\times 10^{-9}$ cm^3 ^{21}Ne per cm^3 of fracture fluid.
336 Greater average excesses over an ASW starting composition are observed in the deeper 2.9 km
337 level samples (1.6 $\times 10^{-8}$ cm^3 ^{21}Ne per cm^3 of fracture fluid) which, like helium, indicates the
338 deeper level contains a larger radiogenic excess. In the Sudbury samples, average radiogenic
339 neon excesses are smaller overall, with Mines 1 and 2 having a ^{21}Ne excess of 1.8 $\times 10^{-9}$ and 1.2
340 $\times 10^{-9}$ cm^3 ^{21}Ne per cm^3 of fracture fluid respectively.

341 The measured isotopes of neon from Table 4 are presented graphically in Figure 3.

342 As seen in Figure 3, samples from Kidd Creek Mine at the deeper level (2.9 km) are even more
343 displaced from initial air ratios (ASW) relative to their 2.4 km counterparts. Indeed, the
344 $^{21}Ne/^{22}Ne$ ratios for the 2.9 km samples are the highest ever measured in crustal samples, free
345 fluids or otherwise (Lippmann-Pipke et al., 2011). As was seen in Holland et al. (2013), the data
346 from this study indicate that fracture fluids in these Precambrian crystalline systems are
347 characterised by a radiogenic $^{20}Ne/^{22}Ne$ end-member that is significantly elevated (red line)
348 compared to what had previously been expected for crystalline rock (black line, Kennedy et al.,
349 1990; Ballentine and Burnard, 2002). The new samples from 2.4 km depth at Kidd Creek Mine
350 (black squares) similarly preserve an elevated crustal production of neon, however, they have
351 somewhat lower $^{21}Ne/^{20}Ne$ and $^{22}Ne/^{20}Ne$ ratios compared to the 2013 study (blue squares) when
352 they were first sampled > 7 years ago. Only the data for Mine 2 from Sudbury lie close to the
353 traditional ASW-crustal mixing line (black line), as did one sample from the Holland et al.

(2013) study. The implications of this data for neon production rate are discussed in Section 5.55.

4.5 Argon

Concentrations of ^{40}Ar are also elevated in all fluid systems due to radiogenic decay of ^{40}K, with concentrations as high as 0.10 cm^3 ^{40}Ar per cm^3 of fracture fluid in the case of the samples from Kidd Creek Mine 2.9 km. Concentrations of ^{40}Ar for the samples from 2.4 km (0.01), and in both Sudbury Mines (0.004 and 0.02 cm^3 ^{40}Ar per cm^3 of fracture fluid respectively) are lower than this, but in all cases the radiogenic component accounts for an extraordinary over 93 % of all ^{40}Ar present.

The 2013 samples reported for 2.4 km had $^{40}Ar/^{36}Ar$ ratios of up to ~44,000, which at the time were the highest crustal values ever measured in a free fluid. In this paper, $^{40}Ar/^{36}Ar$ ratios for samples from the deeper level of Kidd Creek Mine (2.9 km) reach in excess of 125,000 (102,000 average). The resampling of the fluids at 2.4 km depth revealed a lower $^{40}Ar/^{36}Ar$ ratio than in the 2013 study, with an average value of 15,100, compared with the previous average of 31,100. Radiogenic ages based on He, Ne and Ar measurements are discussed in Section 4.10.

While the $^{40}Ar/^{36}Ar$ ratio for the two Sudbury mines are much lower than those in Kidd Creek Mine, an identifiable radiogenic excess from atmospheric ratio (295.5, Ozima and Podosek, 2002) is nonetheless observed. This ratio increases from 4353 in Mine 1 to 17589 in Mine 2. As noted with the ^{40}Ar excess, these high $^{40}Ar/^{36}Ar$ ratios all indicate fluids with a high radiogenic excess relative to the assumed starting composition.

375

376 **4.6 Krypton**

377 All krypton abundances and ratios are given in Appendix A. As ^{80}Kr has no known production
378 pathways within the crust (Ballentine and Burnard, 2002, and references therein) this is typically
379 the isotope chosen for normalisation (in a method analogous to ^{36}Ar normalization discussed
380 above). In this dataset, there are small deviations in $^{78}Kr/^{80}Kr$ and $^{86}Kr/^{80}Kr$ from atmosphere
381 (Table A6), but no correlation with age or mass fractionation trends are observed.

382 **4.7 Xenon**

383 As per the standard approach in noble gas geochemistry, all Xe isotope data are normalised to
384 ^{130}Xe, the Xe isotope with no major radiogenic production pathways (Table 5). Compositions are
385 expressed as in Figure 4 then as deviations relative to ^{130}Xe, and elevated $^{131\text{-}136}Xe/^{130}Xe$ ratios
386 are typical within the crust due to radioactive decay of uranium and plutonium. It is possible to
387 determine the source of radiogenic xenon through comparison with the well-defined fission
388 spectra for each parent radionuclide (Ballentine and Burnard, 2002 and references therein). By
389 anchoring the ^{238}U fission spectra to ^{136}Xe a good agreement is observed between the predicted
390 and observed $^{131\text{-}134}Xe$ excess in the samples (Figure 4). This indicates that the radiogenic xenon
391 excess (Xe*) in all locations can be explained via ^{238}U fission and accumulation of radiogenic Xe
392 over time.

393

394 $^{136}Xe^*$ is greatest in Kidd Creek Mine samples from 2.9 km (9.9×10^{-10} cm^3 ^{136}Xe per cm^3 of
395 fracture fluid) and is an order of magnitude greater than $^{136}Xe^*$ resampled from 2.4 km fluids

396 (7.1 $\times 10^{-10}$ cm^3 ^{136}Xe per cm^3 of fracture fluid). In Sudbury samples, $^{136}Xe^*$ show a smaller
397 range (5.1 $\times 10^{-11}$ and 2.3 $\times 10^{-10}$ cm^3 ^{136}Xe per cm^3 of fracture fluid in Mines 1 and 2
398 respectively), consistent with a lower radiogenic excess in the fluids Mine 2 versus Mine 1 in the
399 Sudbury Basin compared to Kidd Creek Mine fluids.

400 In addition to radiogenic xenon, a small excess over ASW is observed in the 'shielded' ($^{124-}$
401 ^{128}Xe) isotopes which have no significant production within crustal environments (Ballentine and
402 Burnard, 2002). These are given as percentages in Table 8.

403

404 By dividing the percentage deviation by the relative mass difference of the light isotope relative
405 to ^{130}Xe the enrichment in shielded isotopes per amu is calculated. The average enrichment is
406 observed to be the greatest in Kidd Creek Mine samples from 2.9 km (6.7 ‰) followed by Mine
407 2 (3.0 ‰), Kidd Creek Mine samples from 2.4 km (2.6 ‰) and lastly samples from Mine 1 (2.5
408 ‰). As was previously observed in Holland et al. (2013) the light Xe isotopes at both levels of
409 Kidd Creek Mine also show an additional ^{129}Xe excess far beyond that which may be linked by
410 mass fractionation to the $^{124-128}Xe$ excess (Table 8, Figure 5). A ^{129}Xe excess was also observed
411 in 2013 (Holland et al., 2013). The interpretation and implication of this is presented in Section
412 5.33.

413

414 **4.8 Radiogenic noble gases**

415 At Kidd Creek Mine, resampling of previous boreholes from Holland et al. (2013) at 2.4 km
416 depth indicate a reduction in all radiogenically-derived noble gas concentrations expressed as per

417 cm^3 of fracture fluid since initial sampling 44 months prior. In contrast, in the recently completed
418 boreholes sampled immediately after drilling at 2.9 km, the concentrations of noble gases within
419 the fluids are the highest ever reported in the literature. The exception to this is xenon, which
420 shows a similar radiogenic concentration to the samples collected in 2013 from 2.4 km. In both
421 Sudbury mines, a lower excess of radiogenic noble gases is observed per cm^3 of fracture fluid
422 (Table 4).

423 **4.9 Radiogenic residence time calculations**

424 The approach for deriving residence times for fracture fluids is as follows: 1. initial composition
425 of the pore fluids is assumed to be approximately that of seawater at 10 °C with corresponding
426 noble gas content; 2. gas phases are quantitatively recovered from the fluids during sampling; 3.
427 reasonable estimates of combined matrix and fracture porosity (termed bulk porosity here) are
428 applied; 4. noble gases behave conservatively; and 5. all radiogenic noble gases are produced *in*
429 *situ* in a closed system within the crystalline rock formations.

430 In the case of the first assumption, given that the host rock was originally formed within a
431 proximal marine environment (Thurston et al., 2008), it is reasonable to assume the initial pore
432 fluids would be seawater with the corresponding noble gas content. Given the rate at which gas
433 exsolved from the water phase (Table 1), coupled with the known strong affinity of noble gases
434 for a gaseous phase (Crovetto et al., 1982; Ballentine et al., 2002; Warr et al., 2015), total
435 degassing of the water phase can reasonably be ensured during sampling. In addition, degassing
436 processes prior to sampling that affected noble gas concentrations for the samples from Kidd
437 Creek Mine 2.9 km (Figure 2) can be corrected for as seen in Section 4.2. Bulk porosity
438 estimates for crystalline rock of the Canadian Shield vary in a narrow range of ~1 % +/- 0.45 %

with bulk porosity principally existing as fractures within the crystalline rock, decreasing as a function of depth as per Equation 3 (Sherwood Lollar et al., 2014 and references therein). Any gas phase not in solution is expected to occupy negligible volume within these fractures due to the hydrostatic-or-greater pressure of the system (Holland et al., 2013). In contrast, the assumption that all noble gases efficiently migrate into the fluid phase is a simplification at relatively low temperatures, even over up to Ga timescales, but within the closed system assumption means that the derived ages are minimum estimates. Release of the noble gases from the minerals in which they are produced will depend on the mineral size distribution, and both temporal and thermal history (Fulda and Lippolt, 2000; Lippmann et al., 2003; Baxter, 2010; Tolstikhin et al., 2014).

The final assumption is that of a closed system on a connected fracture fluid scale. For the systems presented here we use two lines of evidence to support this assumption. First, the ASW-derived noble gases (^{20}Ne, ^{84}Kr & ^{130}Xe) show reasonable agreement with the assumed starting composition based on ^{36}Ar concentrations (Figure 2). Any noble gas loss/gain through diffusive or bulk gas phase migration in or out of the fracture network would likely result in major elemental fractionation, with neon being the most affected and xenon the least based on their respective diffusivities and differences in the relative partitioning between different phases. As discussed, this trend is not observed in any of the samples in this study (Figure 2). Additionally, any external exchange of noble gases would likely result in variable excesses in the radiogenic noble gases which would be reflected in poorly correlated radiogenic ages between the different noble gas systems (^{4}He*, ^{21}Ne*, ^{40}Ar*, ^{136}Xe*). Crucially this is not observed (Table 9). All residence time estimates are in agreement with one another within error (Table 9), with the exception of some variation outside uncertainty for the estimates derived from ^{21}Ne* that is

462 discussed in the following section. These two lines of evidence support that any exchange with
463 external systems is negligible. Therefore, as in the 2013 study (Holland et al., 2013) all systems
464 presented here are assumed to reflect closed systems on a regional/deposit scale.

465

466 **4.10 Radiogenic Ages**

467 Residence time estimates for fracture fluids are based on resolved radiogenic ^{4}He*, ^{21}Ne*, ^{40}Ar*
468 and ^{136}Xe* that accumulate in subsurface fluids due to radioactive decay of uranium, thorium
469 and potassium over geologic timescales (Ballentine and Burnard, 2002). If these are assumed to
470 have been produced *in situ*, an estimate of the time since isolation can be calculated.

471 The noble gas content per cm^3 of host rock is calculated by multiplying the radiogenic noble
472 gases concentrations per cm^3 of fluid by an estimate of bulk porosity calculated using Equation 3
473 (Sherwood Lollar et al., 2014). This is converted into *in situ* radiogenic noble gas concentration
474 per gram of host rock by dividing this number by typical density of crystalline rock (~2.7 g/cm^3).
475 Using this approach the noble gas content per gram of host rock is obtained. In order to derive
476 residence times, the concentrations of the parent elements for each noble gas were taken from the
477 literature. For Kidd Creek Mine the same Kidd Munro concentrations were used as from Holland
478 et al., 2013 (Th = 9 ± 0.2 ppm, U = 2 ± 0.1 ppm and K = 2 % ± 0.05, based on values taken from
479 Moulton et al., 2011) and for the Sudbury Mines the average tonalite gneiss from the Levack
480 Gneiss Complex was used (Th = 8 ± 0.1 ppm, U = 1 ± 0.2 ppm and K = 1.86 ± 0.05 %, Meldrum
481 et al., 1997). These were combined with the respective decay constants and the total production
482 per decay to estimate production as a function of time. The equations for ^{4}He* and ^{40}Ar*
483 production are as follows:

$$^{4}He^{*} = 8 \times [^{238}U] \times (e^{\lambda 238t} - 1) + 7 \times [^{235}U] \times (e^{\lambda 235t} - 1) + 6 \times [^{232}Th] \times (e^{\lambda 232t} - 1) \quad (1)$$

$$^{40}Ar^{*} = 0.105 \times [^{40}K] \times (e^{\lambda 40t} - 1) \quad (2)$$

where $[^{238}U]$, $[^{235}U]$, $[^{232}Th]$ and $[^{40}K]$ are elemental concentrations in ppm in the host rock, λ_{238}, λ_{235}, λ_{232} and λ_{40} are the decay constants (year^{-1}) 8, 7, 6 are the total atoms of ^{4}He produced from the complete decay chain of each parent radionuclide, 0.105 is the ^{40}K fraction which decays to ^{40}Ar and *t* is time in years (Ballentine and Burnard, 2002; Holland et al., 2013).

As in the previous study (Holland et al., 2013), residence times for both $^{21}Ne^{*}$ and $^{136}Xe^{*}$ were derived using the relationship between $^{4}He^{*}$, $^{21}Ne^{*}$ and $^{136}Xe^{*}$ (9.96×10^{6} and 3.033×10^{8} for $^{4}He^{*}/^{21}Ne^{*}$ and $^{4}He^{*}/^{136}Xe^{*}$ respectively, Ballentine and Burnard, 2002). We assign error bars based on the maximum possible uncertainty associated with this calculation, which is the uncertainty in the bulk porosity estimate (1 % +/- 0.45 % adjusted for depth; Equation 3, after Sherwood Lollar et al., 2014 and references therein) combined in quadrature with the calculated analytical uncertainty and the published analytical uncertainty in the radioelement concentration. These ages and their corresponding 1 σ uncertainty are presented in Table 9 and Figure 6.

From Table 9 it is observed that all fracture fluids residence times agree with one another within uncertainty for boreholes within a given level at Kidd Creek Mine, with no discernible time series. This suggests that, as hypothesized in the conceptual model which we propose in Section 5.2, boreholes from the same level of the mine are intersecting and draining fracture fluids with similar residence times. This is both supported by the similar noble gas isotopic compositions and fluid $\delta^{18}O$ and $\delta^{2}H$ data (Tables 2-8, 10). Accordingly, the method of averaging fluid data

505 for all boreholes for a given mine level, as done in the 2013 study, remains valid for the data in
506 the present study.

507 Based on the averages, the mean residence times of the fluids have decreased for the samples at
508 2.4 km depth at Kidd Creek Mine (0.2 to 0.6 Ga, 0.4 Ga average) since the initial 2013 study (1.1
509 to 1.7 Ga, 1.2 Ga average). This behaviour is consistent with the hydrogeological conceptual
510 model of draining fracture fluids as which was discussed in more detail in Section 5.2.

511 At the deeper (2.9 km) level of Kidd Creek Mine, fluid mean residence times are the oldest yet
512 reported (1.7 Ga average mean residence time). While $^{21}Ne^*$ gives the youngest estimate (1.0
513 Ga), $^{4}He^*$, $^{40}Ar^*$ and $^{136}Xe^*$ estimates are all consistent, with estimates ranging between 1.7 to
514 2.2 Ga. In the case of neon, the average age, calculated using the $^{4}He^*/^{21}Ne^*$ production rate in
515 modern crust, is much lower than its radiogenic counterparts. This is discussed further in Section
516 5.5.

517 While the fluids in both Sudbury mines have significantly younger mean residence times, they
518 are still indicative of systems which have been hydrogeologically isolated over significant
519 periods of time. With estimated mean residence times ranging from 0.2 – 0.6 Ga (Mine 1) and
520 0.2 – 0.9 Ga (Mine 2) these are still older than any previously published systems except for Kidd
521 Creek Mine. Although Mine 1 helium and neon ages are greater than Mine 2, the opposite is
522 observed for argon and krypton. This results in overall average residence times of 0.3 and 0.5 Ga
523 respectively. All ages are presented graphically in Figure 6.

524

525 # 5 Discussion

526 Despite their potential significance in global hydrogen production and deep carbon cycles the
527 volume and distribution of these deep crustal fluids remain poorly constrained. Here the first
528 global estimates of deep crustal reservoirs are calculated as a crucial first step to address this
529 (Section 5.1). A newly-developed conceptual model is also presented in tandem which models
530 distribution, volumes and residence times of fracture fluids within a vertical profile (Section 5.2).
531 This model is expected to provide a much enhanced understanding of fracture fluids on a
532 regional scale. This model is evaluated using both the data generated for this study and
533 previously published data by Holland et al. (2013).

534 In the previously mentioned Holland et al. (2013) study three novel noble gas characteristics
535 were observed: 1. a ^{129}Xe excess attributed to local sediments; 2. a $^{124\text{-}128}Xe$ excess was identified
536 and attributed to an early atmospheric component; and 3. an elevated $^{21}Ne/^{22}Ne$ end-member
537 well above typical crustal values (Holland et al., 2013). In this study three new localities have
538 been identified which clearly preserve fluids on similarly ancient timescales and allow evaluation
539 of the original interpretation of these geochemical features and assess the common elements
540 within other systems. Additionally, the original boreholes at 2.4 km depth at Kidd Mine have
541 been resampled. The geochemical characteristics of each of these are used as the basis to validate
542 key aspects of the proposed conceptual model.

543

544 5.1 Global estimates of deep crustal reservoirs

545 To assess the impact such deep old fracture fluids can have on global cycles it is also essential to
546 have estimates of both their total volume and distribution within the crust. In a recent study
547 Gleeson et al. (2016) used ^{3}H data to estimate the depth penetration of young (< 50-100-year-

548 old) groundwater in the first 2 km of the continental crust, and two-dimensional models of bulk
549 porosity-depth relationships for different crustal rocks integrated with cross-sectional steady-
550 state models of groundwater flow to estimate the global volume of modern groundwater. The
551 analysis yielded the important insight that the volume of modern groundwater (350,000 km^3 to
552 630,000 km^3 for 50 year and 100-year-old water, respectively) is by far the largest component of
553 the planet's active hydrologic cycle (with the exception of the oceans at ~ 1 billion km^3). Given
554 the central role of groundwater in sustaining the Earth's agricultural, social, economic activities,
555 climate and ecosystems, this work generated widespread attention. The even more fundamental
556 corollary of their findings, however, went unnoticed. Specifically, that the ≤ 630,000 km^3 of
557 groundwater that they estimated for modern groundwater (<50-100 years) represents only 1.5 -
558 2.8 % of the total groundwater inventory to 2 km depth (~ 22.6 million km^3; Gleeson et al.,
559 2016). The result is that 97.2 - 98.5 % of groundwater is much older, and we know almost
560 nothing about the age or distribution of that immense "hidden hydrogeosphere" which is not
561 actively interacting with the short-term hydrologic cycle. Similarly, the implications of this deep
562 hydrogeosphere for the habitability of the Earth's crust and for subsurface ecosystems are also
563 poorly constrained.

564 As Gleeson et al. (2016) noted, empirical databases for groundwater, even to 2 km depth, are rare
565 – necessitating a modelling approach to derive even first order estimates of groundwater
566 inventory. No estimate has yet been done on the volume of groundwater beyond this arbitrary 2
567 km cut-off, but a first order estimate can be made here. Below 2 km depth, the bulk of the
568 terrestrial crust is crystalline basement (> 80 % estimated in Gleeson et al. 2016). This estimate
569 is consistent with surface area estimates for the Precambrian crust which indicate crystalline
570 rocks of the Precambrian constitute > 30 % of the exposed continental area at surface and > 72 %

of the bedrock surface area in total for the planet (Goodwin, 1996). Hence, for depths deeper than 2 km in the continental crust we can consider the Precambrian crust as a basis for a representative, but conservative, estimate for determining the groundwater inventory at depth. Including younger Paleozoic crystalline rocks would only increase this estimate and therefore can be neglected for this first order analysis.

Given the total surface area of the continents is 1.48×10^8 km^2 and knowing that 72 % of that crust is Precambrian crystalline rock (1.06×10^8 km^2; Goodwin, 1996), we can calculate the volume of groundwater in the crust to depth by incorporating bulk porosity estimates. Measured values of bulk porosity within fractures for crystalline basement rocks range from 0.1 to 2.3 % (Aquilina et al., 2004; Stober, 1997; Stober and Bucher, 2007) with a mean of 1 % ± 0.45 % (2 σ) (Bucher and Stober, 2010). Due to the limited number of such empirical measurements, Sherwood Lollar et al. (2014) took a modelling approach and estimate bulk porosity that exponentially declines with depth after the models of Bethke (1985). The equation is given as:

$$\Phi = (1.6e^{-z/4.8})/100 \quad (3)$$

where ϕ is bulk porosity (%) and z is depth (km). To 10 km depth, this approach predicts an average bulk porosity of 0.96 %, consistent with the above measurements from the literature and the value used by Gleeson et al. (2016) for crystalline rocks of the upper crust.

The depth of water-filled fractures in the crust is more uncertain. At > 15 km depth, temperatures are likely too warm for brittle faulting and ductile creep persists (Sleep and Zoback, 2007). To at least 10 km however, brittle crust faults should contain water, likely under hydrostatic pressure (Townend and Zoback, 2000 and references therein). Using the surface area of Precambrian crystalline rock, an average bulk porosity of 1 %, to a depth of 10 km then, suggests another 8.5

593 million km^3 should be added to the groundwater inventory in addition to the 22.6 million km^3
594 estimated for the top 2 km (Gleeson et al., 2016). This indicates that fluids residing in
595 Precambrian crystalline basement may account for somewhere in the region of 30 % of the total
596 groundwater inventory of the earth. The residence times of this total groundwater inventory of >
597 30 million km^3 is, to date, almost completely unknown. This study represents an important first
598 step in addressing this gap through defining an approach for estimating the mean residence times
599 of such fluids and expanding beyond the earlier study at Kidd Creek Mine to demonstrate that
600 such ancient fluids (Ma to Ga) are a characteristic feature of the Precambrian deep crust.

601

602 **5.2 Conceptual model**

603 Based on this study and previous investigations of saline fracture fluids in the deep Precambrian
604 cratons (Sherwood Lollar et al., 2007; Lippman-Pipke et al., 2011; Holland et al., 2013), the
605 following conceptual model has been developed to better constrain distribution, volumes and
606 residence times of fracture fluids within a vertical profile (Figure 7). Fracture fluids in deep
607 crystalline rock decrease in frequency and are increasingly hydrogeologically isolated one from
608 another with increasing depth in the crust (Sleep and Zoback, 2007; Golders Associates 2010).
609 Based on the results of Holland et al (2013), it is reasonable to assume that the deeper, more
610 hydrogeologically isolated fractures contain fluids with the oldest residence times, and as a
611 corollary, that less deep fractures will contain a larger volume of fluids with relatively less
612 ancient residence time distributions.
613 Within the host rocks investigated in this study, the discrete fracture systems contain highly
614 saline fluids and dissolved gases under pressure. The distribution of these fractures are the
615 dominant control on bulk porosity and associated permeability. The fractures are highly variable

616 in terms of geometry, spacing and structure which results in high variations in bulk porosity,
617 permeability and fluid volume locally. While a few studies exist in Precambrian rock where the
618 actual fracture distribution have been mapped (Manzi et al., 2012); such information is not
619 typically available and does not exist for the sites investigated in this study. Conceptually
620 however, it is clear that individual boreholes drilled into the crystalline rock intersect one or
621 more these fracture networks, providing a means for the host fluids to migrate out of the host
622 rock and any given borehole will intersect multiple fractures (Figure 7). Accordingly, the fluids
623 sampled from each borehole are the sum total of all fluids being discharged from each
624 contributing fracture. With each fracture containing fluids of possibly different geological
625 residence times, the resulting noble gas-derived mean residence time for the samples collected at
626 the borehole collar thus represents the mean residence time of all fluids contributing to the
627 fracture flow. The borehole-specific mean residence times are dependent on the isolation age, the
628 volumes and the fluid discharge rates for each contributing fracture. Where boreholes intersect
629 the same fracture networks, this will result in similar geochemistry and residence times. This
630 model for fractured rock is analogous to those applied to unconsolidated porous media in the
631 sense that any groundwater is a composite reservoir contributed to from multiple flowlines with a
632 certain degree of heterogeneity in provenance and age as a function of the hydrogeological
633 setting (Bethke and Johnson, 2008; Goode, 1996). This “mixed reservoir” aspect of any
634 hydrogeologic system is amplified for fractured rock systems due to the high degree of
635 heterogeneity inherent to fractured rock (Golders Associates 2010). Over time, stress regimes
636 within the host rock change, and in the tectonically quiescent rocks of the Precambrian Shields
637 this is primarily caused by large scale, regional stress variations (Sleep and Zoback, 2007). Stress
638 changes on a regional scale may result in both reactivation of pre-existing planes of weakness

639 and the development of new, localised fractures. Localised changes to the stress regime may
640 additionally be produced due to mining activity. Through all of these processes new, fluid-
641 bearing fractures are expected to contribute to the sampling boreholes over time. Since the
642 preservation potential of these fracture networks is expected to be lower as a function of
643 increasing age, statistically these fluids are likely to be representative of younger residence
644 times.
645
646 As a result mean residence times may also change, as some fractures drain out and contribute
647 less to the overall volume discharging form the boreholes while new ones become connected.
648 Based on these considerations the new investigation at Kidd Creek Mine allows assessment of
649 two hypotheses: a. that resampling of the Holland et al 2013 boreholes would show less ancient
650 mean residence times as the contribution from the more older, isolated fractures decreased over
651 time; and b. the new deeper boreholes at 2.9 km would provide fluid mean residence times
652 comparable to or even older than those of the Holland at al. 2013 study (Sleep and Zoback, 2007;
653 Townend and Zoback, 2000). Where applicable we evaluate these hypotheses in the remainder of
654 the discussion section using the geochemical data presented in this study.
655
656 One final point to consider within the conceptual model is the potential for natural bias within
657 the sampled fluids which may too have a bearing on the calculated residence times. In this kind
658 of environment fluids are principally considered to exist within fractures, rather than at grain
659 boundaries or as fluid inclusions. The mean residence times of the fluids are therefore net
660 combination of all fractures sampled. However, it is reasonable to consider that the larger
661 fractures are more likely to be intersected by an exploratory borehole than their smaller-scale

662 counterparts. Given that a relationship between fluid volume and residence time may exist (as
663 hypothesised here) there may be a biasing towards boreholes sampling younger, rather than older
664 fluids at any given level. Accordingly the mean residence times presented here would remain
665 conservative estimates, even if there is a natural bias present in the fluids being sampled.
666

667 **5.3 ^{129}Xe anomaly**

668 In the 2013 study a ^{129}Xe excess far in excess of any early atmosphere component or possible
669 mantle component was identified in the fractures waters at Kidd Creek Mine. This was attributed
670 to a radiogenic ^{129}Xe excess produced from ^{129}I likely sorbed to the carbon-rich formations of the
671 Kidd Creek Mine deposit during deposition in a proximal seafloor environment. Preservation of
672 the ^{129}Xe results from decay of ^{129}I was attributed to rapid periods of intense volcanism that
673 quickly capped the sedimentary layers – creating a closed system in which ^{129}I (and resulting
674 ^{129}Xe) were sequestered (Holland et al., 2013). In this study an even greater ^{129}Xe/^{130}Xe excess is
675 identified in the fluids from 2.9 km at Kidd Creek Mine. The increase in ^{129}Xe/^{130}Xe ratios
676 however is small compared to the ^{136}Xe/^{130}Xe ratio. In contrast, a very large ^{136}Xe/^{130}Xe
677 deviation is observed from 21 % to 87 % (i.e. 4.1 ± 0.5 times higher in the 2.9 km samples
678 versus those from 2.4 km). The ^{129}Xe/^{130}Xe only increases from 1.2 % to 3.8 % (3.3 ± 0.6 times
679 higher. Though these values lie within uncertainty of one another, based on standard deviation,
680 when standard error is calculated (which can be used in this case to evaluate the accuracy of the
681 mean value) these values lie outside of uncertainty of one another (4.1 ± 0.2 & 3.3 ± 0.3)
682 indicating the average increases are distinct for these two isotopes.

683 This lack of proportional co-variation between the radiogenic ^{136}Xe, and sedimentary-derived
684 ^{129}Xe, is not consistent with a single homogenised ancient fluid of uniform age (containing the
685 ^{129}Xe excess) mixing variably with a single modern fluid component to produce the observed
686 excesses. Instead, this supports the interpretation that boreholes at 2.4 km and 2.9 km sample
687 different fracture systems, consistent with the proposed conceptual model of hydrogeologically
688 isolated fracture networks preserving fluids of different provenance and age. As a result,
689 different ^{129}Xe and ^{136}Xe excesses in the fluids could result from variances in the ^{129}Xe excess
690 (due to different degrees of water-rock interaction), coupled with an isolation age-dependent
691 $^{136}Xe^*$ component.

692

693 In contrast to the Kidd Creek Mine fluids, no ^{129}Xe excess is observed in either of the two
694 Sudbury mines. Given that the Sudbury Basin system was the loci of a major bolide impact at 1.8
695 Ga, massively fracturing the terrain on a regional scale over hundreds of km, the absence of the
696 ^{129}Xe excess observed at the well-preserved Kidd Creek Mine deposit was expected. This
697 highlights the ability of noble gases to discern between the distribution of fracture fluids of
698 different age and provenance as a function of different geologic settings.

699

700 **5.4 Ancient atmospheric signal**

701 A fractionated excess in the shielded xenon isotopes ($^{124\text{-}128}Xe$) relative to modern air values is
702 present in ancient fracture fluids and may also be present in the $^{131\text{-}136}Xe$ isotopes (Appendix C).
703 These cannot be explained using any known xenon production pathways or *in situ* mass
704 fractionation processes (which would affect all xenon isotopes) and have previously been

attributed to atmospheric Xe loss over geological time by ionisation of xenon in the early atmosphere (Pujol et al., 2009; Pujol et al., 2011, Avice 2014). This has been used as basis for resolving the 'xenon paradox'; the observation that Earth has ~90 % lower Xe abundance than predicted by meteorite and Solar abundance patterns (Anders and Owen, 1977; Podosek and Ozima, 2000; Pepin and Porcelli, 2002). The atmosphere Xe loss model has been used to derive an atmospheric isotopic evolution curve for xenon, from an initial Xe-U/solar composition evolving to modern values (Pujol et al., 2011; Holland et al., 2013; Avice and Marty, 2014). The exact mechanisms and rates involved in this isotopic fractionation and loss are presently poorly constrained (Avice and Marty, 2014; Hébrard and Marty, 2014). Current models are exclusively based on xenon data from fluid inclusions (e.g. Pujol et al., 2011; Avice and Marty, 2014), the majority of which are greater than 2 Ga (Hébrard and Marty, 2014). To date, data covering the 2 Ga – present day timescale is sparse. Expanding the dataset to cover this range will allow for better constraints on the rates and timing of the xenon isotopic evolution of the Earth's atmosphere over planetary timescales; and identification of the mechanism that may control any such process (Hébrard and Marty, 2014). To investigate this aspect of atmospheric Xe in the light of the samples in this study, Figure 5 (and Table 8) show the data for all the light excesses of Xe relative to modern atmosphere.

An average $^{124\text{-}128}$Xe excess is observed for all samples (Figure 5). Once again samples from 2.9 km depth show the largest excesses, while the resampled fracture fluids at 2.4 km show a smaller excess compared to the initial 2013 observation. This trend is in agreement with a hydrogeologic conceptual model which predicts that due to fractures draining over time a younger mean residence time will be observed in these boreholes, as well as either a lower (or even no) $^{124\text{-}128}$Xe excess. This model is summarised in Section 5.2. This is because exact $^{124\text{-}128}$Xe excess

present within a fracture fluid is dependent on three key factors; 1. the rates, evolution and termination of the process driving this fractionation, 2. The point at which the fracture fluid became isolated from the early atmosphere and, 3 the relative proportion of each fracture fluid component within the fracture network.

The presence of a resolvable $^{124\text{-}128}$Xe excess in the Sudbury system fluids is of particular interest. These are the fluids with the youngest mean residence times (0.3-0.5 Ga) in which such a signal has been identified and indicates that at both locations one or more of the oldest fracture fluid components (which combined yield the mean residence times) contain an early atmospheric Xe signal. In addition we argue that the concept of such shallow (<2 km) fractures preserving fluids from before the SIC-forming impact event is unrealistic. This is due to the magnitude and scope of the event which is the second largest impact identified globally and caused ejecta to spread over at least a 650 km radius (Grieve and Therriault, 2000; Jirsa et al., 2011). Any fluid components in either Sudbury mine are therefore likely younger than the impact event at 1.85 Ga. The implication of this is that the fractionation mechanisms proposed to create the $^{124\text{-}128}$Xe anomalies noted in previous literature must in fact have continued beyond 2 Ga and has been preserved in one or more fluid components. These fluid components, likely combined with younger fluids, have subsequently resulted in the calculated mean residence times 0.3 & 0.5 Ga for the two Sudbury mines. The identification of an early atmospheric Xe component in fluids younger than 1.85 Ga is more consistent with models which indicate ionisation of the atmospheric Xe continuing until more recently (Pujol et al., 2011; Hébrard and Marty, 2014) rather than those which suggest it ended earlier than 2 Ga (Avice and Marty, 2014). Further investigation of this novel type of sample containing early atmospheric Xe components in

addition to the traditional reliance on fluid inclusions, will allow better evaluation of alternative Xe loss mechanisms such as hydro-dynamic escape (Pepin, 2000).

5.5 Ancient neon signal

Nucleogenic neon in Precambrian systems have recently been shown to have a distinct $^{21}Ne/^{22}Ne$ end-member ($^{21}Ne/^{22}Ne$ = 3.1 – 3.5 at the $^{20}Ne/^{22}Ne$ intercept) compared to the canonical values previously observed for the crust (Kendrick et al., 2011; Lippmann-Pipke et al., 2011; Holland et al, 2013). Typically nucleogenic $^{21}Ne/^{22}Ne$ end-members have values of 0.47 - 0.79 at the $^{20}Ne/^{22}Ne$ intercept for modern crustal production (Kennedy et al., 1990; Ballentine and Burnard, 2002). Given that nucleogenic neon is produced via $^{17,18}O(\alpha,n)^{20,21}Ne$, $^{19}F(\alpha,n)^{22}Na(\beta^{+})^{22}Ne$ and $^{19}F(\alpha,p)^{22}Ne$ (Wetherill, 1954), the dominant control on $^{21}Ne/^{22}Ne$ production is the ratio of oxygen to fluorine (O/F) in the proximity of U and Th-derived α particles (~40 μm Wetherill, 1954; Kennedy et al, 1990; Ballentine 1997; Ballentine and Burnard, 2002). In modern crust, $^{21}Ne/^{22}Ne$ production rates are lower by a factor of ~8 based on that predicted by average O/F ratios (Kennedy et al, 1990; Ballentine 1997; Ballentine and Burnard, 2002; Lippmann-Pipke et al., 2011). This has been interpreted as a relative localised enrichment of F within Th and U-bearing minerals resulting in a greater ^{22}Ne production than expected based on the bulk ratios (Kennedy et al., 1990). In Precambrian rocks, however, depletion in F has been observed resulting in bulk O/F ratios being elevated by roughly an order of magnitude (Lippmann-Pipke et al., 2011). This relative F deficit, resulting in reduced ^{22}Ne production, has been suggested as the potential cause for the elevated $^{21}Ne/^{22}Ne$ $^{21}Ne/^{22}Ne$ end-member values > 3 observed for the first time in the fracture waters of the South African gold mines (Lippmann-Pipke et al., 2011).

772 In this study, with the exception of Mine 2, all fluid samples also show elevated $^{21}Ne/^{22}Ne$
773 relative to $^{20}Ne/^{22}Ne$ (Figure 3). Lippmann-Pipke et al. (2011) attributed this to release of Ne-
774 rich fluid inclusions from an earlier Precambrian source into the sampled younger fracture fluids
775 (Lippmann-Pipke et al., 2011). However, in the case of Kidd Creek Mine, a similar explanation
776 (fluid inclusion leakage) would require significant volumes of fluid addition from inclusion
777 given the large volumes of water produced from these fracture fluid networks (Holland et al.,
778 2013; Table 1). The simplest explanation is that the nucleogenic $^{21}Ne/^{22}Ne$ is a component of the
779 original fracture fluids and has been produced based on the average O/F ratios within ~40 μm of
780 any α emitters (U & Th) within the host rock. This average O/F ratio within would need to be
781 greater than that of the modern crust by a factor of 4.9. This is lower than that observed by
782 Lippmann-Pipke et al. (11.9) in rocks aged between 2.7 – 3.1 Ga. Although a speculative
783 relationship between age and evolving $^{21}Ne/^{22}Ne$ crustal production ratios might be inferred, this
784 difference may also simply reflect the specific formation histories and mineralogy of each
785 locality and warrants further investigation.

786

787 **5.6 Temporal evolution in the context of a hydrogeologic conceptual model for fracture**
788 **networks**

789 This study provides the longest temporal record of deep fracture fluids published to date. The
790 resampling of 2.4 km depth after 44 months provides insight into the temporal evolution of this
791 system. All radiogenic excesses per cm^3 of fluid decreased and radiogenic/non-radiogenic ratios
792 evolved towards ASW ratios. In the case of ^{4}He, average abundances per cm^3 of fluid decreased
793 by a factor of 1.85. At the same time the $^{40}Ar/^{36}Ar$ ratio and the $^{136}Xe/^{130}Xe$ % deviation

794 decreased by factors of 2.07 and 1.86 respectively. In the case of neon a vector-based approach is
795 applied. For this, the shift of each average $^{20}Ne/^{22}Ne$ & $^{21}Ne/^{22}Ne$ from the starting (ASW)
796 composition was calculated and combined using the formula $a^2 + b^2 = c^2$. By dividing the
797 combined value from the original study by the resampled combined value from the data
798 presented here the relative decrease in radiogenic isotopes is quantified. This reveals a radiogenic
799 reduction by a factor of 1.95 which is in line with that of the other isotope systems.

800 This consistent reduction of all noble gas excesses indicates a bulk (i.e. unfractionated) change in
801 the mixing ratio between the initial ancient end-member composition as documented in Holland
802 et al. (2013) and a less ancient component resulting in reduction in mean residence times. δ^2H
803 and $\delta^{18}O$ values continue to rule out any modern meteoric fluid component impacting these
804 samples (Table 10, Figure 8). Hence this secondary fluid must represent younger, but still old
805 fluids discharging from the fracture network and contributing to the overall fluid discharging at
806 the borehole collar (point of sampling). Such fluid evolution is consistent with the proposed
807 conceptual model (Section 5.2).

808

809

810 **6 Summary/conclusions**

811 This work highlights that the isolated ancient fluid system discovered at 2.4 km depth in 2013 is
812 not unique. We have expanded from this initial discovery to include three additional isolated
813 fluid systems with average mean residence times spanning from 0.3 to 1.7 Ga.

The deeper level at Kidd Mine reveal the oldest mean fluid residence times ever encountered in free fluids (1.7 Ga). The resampled 2.4 km meanwhile indicates the addition of younger, yet still old fracture fluids, consistent with the conceptual model for these types of system. As the distance between the two levels is sufficient for the fluids to be isotopically distinct from one another, isolation between the two levels can be inferred. This gives additional constraints over the maximum size of the fluid reservoirs contributing to each system. The isolation occurred earlier for the deeper level based on radiogenic and early atmospheric ages which also fits with the proposed conceptual model. Outside of Kidd Mine the two new mines in the Sudbury system both indicate younger mean fluid residence times (0.3 Ga and 0.5 Ga for Mine 1 & 2 respectively) revealing the presence of 'meso-age' systems as well as the truly ancient. In all localities, a shielded xenon anomaly is present which has typically been attributed to an early atmosphere component. Given the timing of the Sudbury impact, which puts a maximum age on the oldest fluid component within these two mine systems (1.849 Ga), this work therefore reveals the process which fractionated xenon was still in operation beyond 2 Ga.

The discovery of each additional system suggests that ancient fluids may be far more pervasive within the deep crust than originally thought. Consequently, their occurrence needs to be more extensively documented, and quantitatively estimated. Future noble gas studies can identify additional ancient fluid systems, assess the volumes involved and determine the degree of hydrogeologic connection or isolation, from surface systems. Crucially though, the noble gases provide a temporal timeframe which can be combined with additional noble gas, stable isotope and biological investigation to glean insight into the geochemical and biological evolution of our planet.

7 Acknowledgements

This study was supported by the Canada Research Chairs program, Natural Sciences and Engineering Research Council of Canada Discovery and Accelerator grants, and additional funding from the Deep Carbon Observatory and Nuclear Waste Management Agency. Thanks are due to colleagues and supporters at the mines whose efforts and support for the sampling program were invaluable.

8 References

Anders E. and Owen T. (1977) Mars and Earth: Origin and Abundance of Volatiles. *Science* 198, 453-465.

Aquilina, L., de Dreuzy, J.-R., Bour, O. and Davy, P. (2004) Porosity and fluid velocities in the upper continental crust (2 to 4 km) inferred from injection tests at the Soultz-sous-Forêts geothermal site. *Geochimica et Cosmochimica Acta* 68, 2405-2415.

Avice, G. and Marty, B. (2014) The iodine-plutonium-xenon age of the Moon-Earth system revisited. *Philosophical Transactions of the Royal Society a-Mathematical Physical and Engineering Sciences* 372.

Ballentine, C.J., Burgess, R. and Marty, B. (2002) Tracing fluid origin, transport and interaction in the crust *in* Porcelli, D., Ballentine, C. J., & Wieler, R. (Eds.), Noble Gases in Geochemistry and Cosmochemistry. Reviews in Mineralogy and Geochemistry. Mineralogical Society of America, pp. 539-614.

Ballentine, C.J. and Burnard, P.G. (2002) Production, release and transport of noble gases in the continental crust *in* Porcelli, D., Ballentine, C. J., & Wieler, R. (Eds.), Noble Gases in Geochemistry and Cosmochemistry. Reviews in Mineralogy and Geochemistry. Mineralogical Society of America, pp. 481-538.

Ballentine, C.J. and Hall, C.M. (1999) Determining paleotemperature and other variables by using an error-weighted, nonlinear inversion of noble gas concentrations in water. *Geochimica et Cosmochimica Acta* 63, 2315-2336.

Ballentine C. J. (1997) Resolving the mantle He/Ne and crustal 21Ne/22Ne in well gases. *Earth and Planetary Science Letters* 152, 233–249.

Ballentine C. J., Onions R. K., Oxburgh E. R., Horvath F. and Deak J. (1991) Rare gas constraints on hydrocarbon accumulation, crustal degassing and groundwater flow in the Pannonian Basin. *Earth and Planetary Science Letters* 105, 229–246.

Barry P. H., Lawson M., Meurer W. P., Warr O., Mabry J. C., Byrne D. J. and Ballentine C. J.

(2016) Noble gases solubility models of hydrocarbon charge mechanism in the Sleipner Vest gas field. *Geochimica Et Cosmochimica Acta* 194, 291–309.

Baxter, E.F. (2010) Diffusion of Noble Gases in Minerals. *Reviews in Mineralogy and Geochemistry* 72, 509-557.

Berger, B.R., Bleeker, W., van Breemen, O., Chapman, J.B., Peter, J.M., Layton-Matthews, D. and Gemmell, J.B. (2011) Results from the Targeted Geoscience Initiative III Kidd–Munro Project. Open File Report 6258.

Bethke, C.M. (1985) A numerical model of compaction-driven groundwater flow and heat transfer and its application to the paleohydrology of intracratonic sedimentary basins. *Journal of Geophysical Research: Solid Earth* 90, 6817-6828.

Bethke, C.M. and Johnson, T.M. (2008) Groundwater age and groundwater age dating. Annual Review of Earth and Planetary Sciences 36, 121-152.

Bleeker, W. and Parrish, R.R. (1996) Stratigraphy and U-Pb zircon geochronology of Kidd Creek: Implications for the formation of giant volcanogenic massive sulphide deposits and the tectonic history of the Abitibi greenstone belt. *Canadian Journal of Earth Sciences* 33, 1213-1231.

Bucher, K. and Stober, I. (2010) Fluids in the upper continental crust. *Geofluids* 10, 241-253.

Card K. D. (1994) Geology of the Levack gneiss complex, the northern footwall of the Sudbury structure, Ontario., Geological Survey of Canada.

Chivian, D., Brodie, E.L., Alm, E.J., Culley, D.E., Dehal, P.S., DeSantis, T.Z., Gihring, T.M., Lapidus, A., Lin, L.H., Lowry, S.R., Moser, D.P., Richardson, P.M., Southam, G., Wanger, G., Pratt, L.M., Andersen, G.L., Hazen, T.C., Brockman, F.J., Arkin, A.P. and Onstott, T.C. (2008) Environmental genomics reveals a single-species ecosystem deep within earth. *Science* 322, 275-278.

Crovetto, R., Fernandez-Prini, R. and Japas, M.L. (1982) Solubilities of inert gases and methane in H_2O and in D_2O in the temperature range of 300 to 600 K. *Journal of Chemical Physics* 76, 1077-1088.

Davis, D.W. (2008) Sub-million-year age resolution of Precambrian igneous events by thermal extraction-thermal ionization mass spectrometer Pb dating of zircon: Application to crystallization of the Sudbury impact melt sheet. *Geology* 36, 383-386.

Davis D. W., Schandl E. S. and Wasteneys H. A. (1994) U-Pb dating of minerals in alteration halos of Superior Province massive sulfide deposits: syngenesis versus metamorphism. *Contributions to Mineralogy and. Petrology* 115, 427–437.

Etiope G. and Sherwood Lollar B. (2013) Abiotic methane on earth. *Reviews of Geophyics* 51, 276–299.

Frape S. K., Fritz P. and Mcnutt R. H. (1984) Water Rock Interaction and Chemistry of Groundwaters from the Canadian Shield. *Geochimica et Cosmochimica Acta* 48, 1617–1627.

Fulda, C. and Lippolt, H.J. (2000) Diffusion coefficients of noble gases in natural minerals: An apparent experimental time dependence caused by domain size spectra. Mathematical *Geology* 32, 31-47.

Gleeson, T., Befus, K.M., Jasechko, S., Luijendijk, E. and Cardenas, M.B. (2016) The global volume and distribution of modern groundwater. *Nature Geoscience* 9, 161-167.

Goode, D.J. (1996) Direct simulation of groundwater age. *Water Resources Research* 32, 289-296.

Goodwin, A.M. (1996) Chapter 1 - Distribution and Tectonic Setting of Precambrian Crust, Principles of Precambrian Geology. Academic Press, London, pp. 1-50.

Graham, D.W. (2002) Noble gas isotope geochemistry of Mid-Ocean Ridge and Ocean Island Basalts: Characterization of mantle source reservoirs *in* Porcelli, D., Ballentine, C. J., & Wieler, R. (Eds.), Noble Gases in Geochemistry and Cosmochemistry. Reviews in Mineralogy and Geochemistry. Mineralogical Society of America.

Grieve R. and Therriault A. (2000) Vredefort, Sudbury, Chicxulub: three of a kind? *Annual Review of Earth and Planetary Sciences* 28, 305–338.

Hébrard, E. and Marty, B. (2014) Coupled noble gas–hydrocarbon evolution of the early Earth atmosphere upon solar UV irradiation. *Earth and Planetary Science Letters* 385, 40-48.

Holland, G., Sherwood Lollar, B., Li, L., Lacrampe-Couloume, G., Slater, G.F. and Ballentine, C.J. (2013) Deep fracture fluids isolated in the crust since the Precambrian era. *Nature* 497, 357.

James R. S. and Golightly J. P. (2009) Metamorphism and Metasomatism. *In* A Field Guide to the Geology of Sudbury (eds. D. Rousell and G. H. Brown).

Jirsa M. A., Fralick P. W., Weiblen P. W. and Anderson J. L. B. (2011) Sudbury impact layer in the western Lake Superior region. Field Guide. 24, 147–169.

Kendrick M. A., Honda M., Walshe J. and Petersen K. (2011) Fluid sources and the role of abiogenic-CH4 in Archean gold mineralization: Constraints from noble gases and halogens. *Precambrian Research* 189, 313–327.

Kennedy, B.M., Hiyagon, H. and Reynolds, J.H. (1990) Crustal neon: A striking uniformity. *Earth and Planetary Science Letters* 98, 277-286.

Kietäväinen, R. and Purkamo, L. (2015) The origin, source, and cycling of methane in deep crystalline rock biosphere. *Frontiers in Microbiology* 6, 725.

Kipfer, R., Aeschbach-Hertig, W., Peeters, F. and Stute, M. (2002) Noble gases in lakes and ground waters *in* Porcelli, D., Ballentine, C. J., & Wieler, R. (Eds.), Noble Gases in Geochemistry and Cosmochemistry. Reviews in Mineralogy and Geochemistry. Mineralogical Society of America, pp. 615-700.

Krogh T. E., Davis D. W. and Corfu F. (1984) Precise U-Pb zircon and baddeleyite ages for the Sudbury area. In The geology and ore deposits of the Sudbury structure Ontario: Ontario Geological Survey. pp. 431–446.

Lau M. C. Y., Kieft T. L., Kuloyo O., Linage-Alvarez B., van Heerden E., Lindsay M. R., Magnabosco C., Wang W., Wiggins J. B., Guo L., Perlman D. H., Kyin S., Shwe H. H., Harris R. L., Oh Y., Yi M. J., Purtschert R., Slater G. F., Ono S., Wei S., Li L., Sherwood Lollar B. and

949 Onstott T. C. (2016) An oligotrophic deep-subsurface community dependent on syntrophy is
950 dominated by sulfur-driven autotrophic denitrifiers. *Procedings of the Natural Academy of*
951 *Science* 113, E7927–E7936.

952 Li L., Wing B. A., Bui T. H., McDermott J. M., Slater G. F., Wei S., Lacrampe-Couloume G.
953 and Sherwood Lollar B. (2016) Sulfur mass-independent fractionation in subsurface fracture
954 waters indicates a long-standing sulfur cycle in Precambrian rocks. *Nature Communications* 7.

955 Lin, L.H., Wang, P.L., Rumble, D., Lippmann-Pipke, J., Boice, E., Pratt, L.M., Sherwood Lollar,
956 B., Brodie, E.L., Hazen, T.C., Andersen, G.L., DeSantis, T.Z., Moser, D.P., Kershaw, D. and
957 Onstott, T.C. (2006) Long-term sustainability of a high-energy, low-diversity crustal biome.
958 *Science* 314, 479-482.

959 Lippmann-Pipke, J., Sherwood Lollar, B., Niedermann, S., Stroncik, N.A., Naumann, R., van
960 Heerden, E. and Onstott, T.C. (2011) Neon identifies two billion year old fluid component in
961 Kaapvaal Craton. *Chemical Geology* 283, 287-296.

962 Lippmann, J., Stute, M., Torgersen, T., Moser, D.P., Hall, J.A., Lin, L., Borcsik, M., Bellamy,
963 R.E.S. and Onstott, T.C. (2003) Dating ultra-deep mine waters with noble gases and ^{36}Cl,
964 Witwatersrand Basin, South Africa. *Geochimica Et Cosmochimica Acta* 67, 4597-4619.

965 Long, D.G.F. (2009) The Huronian Supergroup, in: Rousell, D., Brown, G.H. (Eds.), A Field
966 Guide to the Geology of Sudbury. Ontario Geological Survey.

967 Magnabosco, C., Ryan, K., Lau, M.C.Y., Kuloyo, O., Sherwood Lollar, B., Kieft, T.L., van
968 Heerden, E. and Onstott, T.C. (2016) A metagenomic window into carbon metabolism at 3km
969 depth in Precambrian continental crust. *ISME Journal* 10, 730-741.

970 Mamyrin B. A., Anufriyev G. S., Kamensky I. L. and Tolstikhin I. N. (1970) Determination of
971 the isotopic composition of atmospheric helium. *Geochemistry International*, 498–505.

972 Manzi M., Durrheim R. J., Hein K. A. A. and King N. (2012) 3D edge detection seismic
973 attributes used to map potential conduits for water and methane in deep gold mines in the
974 Witwatersrand basin, South Africa. *Geophysics* 77, 133-147.

975 Meldrum, A., AbdelRahman, A.F.M., Martin, R.F. and Wodicka, N. (1997) The nature, age and
976 petrogenesis of the Cartier batholith, northern flank of the Sudbury structure, Ontario, Canada.
977 *Precambrian Research* 82, 265-285.

978 Moulton B. J. A., Fowler A. D., Ayer J. A., Berger B. R. and Mercier-Langevin P. (2011)
979 Archean subqueous high-silica rhyolite coulées: Examples from the Kidd-Munro Assemblage in
980 the Abitibi Subprovince. *Precambrian Research* 189, 389–403.

981 Onstott T. C., Hinton S. M., Silver B. J. and King H. E. (2010) Coupling hydrocarbon
982 degradation to anaerobic respiration and mineral diagenesis: Theoretical constraints. *Geobiology*
983 8, 69–88.

984 Ozima, M. and Podosek, F.A. (2002) Noble Gas Geochemistry, Second Edition ed. Cambridge
985 University Press.

986 Pattison E. F. (2009) Sudbury Igneous Complex. *In* A Field Guide to the Geology of Sudbury
987 (eds. D. Rousell and G. H. Brown).

988 Pedersen M., Iversen S., Sorensen K. and Johansen E. (2005) The long and winding road from

989 the research laboratory to industrial applications of lactic acid bacteria. FEMS Microbiol. Rev.
990 29, 611–624.

991 Pepin R. O. and Porcelli D. (2002) Origin of noble gases in the terrestrial planets in Porcelli, D.,
992 Ballentine, C. J., & Wieler, R. (Eds.). *In* Noble Gases in Geochemistry and Cosmochemistry.
993 Reviews in Mineralogy and Geochemistry Mineralogical Society of America. pp. 191–246.

994 Pepin, R.O. (2000) On the Isotopic Composition of Primordial Xenon in Terrestrial Planet
995 Atmospheres. *Space Science Reviews* 92, 371-395.

996 Podosek F. A. and Ozima M. (2000) The xenon age of the Earth. *Origin of the Earth and Moon*
997 1, 63–72.

998 Pujol, M., Marty, B. and Burgess, R. (2011) Chondritic-like xenon trapped in Archean rocks: A
999 possible signature of the ancient atmosphere. *Earth and Planetary Science Letters* 308, 298-306.

1000 Pujol, M., Marty, B., Burnard, P. and Philippot, P. (2009) Xenon in Archean barite: Weak decay
1001 of 130Ba, mass-dependent isotopic fractionation and implication for barite formation.
1002 *Geochimica et Cosmochimica Acta* 73, 6834-6846.

1003 Sherwood Lollar, B., Onstott, T.C., Lacrampe-Couloume, G. and Ballentine, C.J. (2014) The
1004 contribution of the Precambrian continental lithosphere to global H_2 production. *Nature* 516,
1005 379-382.

1006 Sherwood Lollar, B. and Ballentine, C.J. (2009) Insights into deep carbon derived from noble
1007 gases. *Nature Geoscience* 2, 543-547.

1008 Sherwood Lollar B., Voglesonger K., Lin L.-H., Lacrampe-Couloume G., Telling J., Abrajano T.
1009 A., Onstott T. C. and Pratt L. M. (2007) Hydrogeologic controls on episodic H2 release from
1010 Precambrian fractured rocks—energy for deep subsurface life on Earth and Mars. *Astrobiology*
1011 7, 971–986.

1012 Sherwood Lollar, B., Lacrampe-Couloume, G., Slater, G.F., Ward, J., Moser, D.P., Gihring,
1013 T.M., Lin, L.H. and Onstott, T.C. (2006) Unravelling abiogenic and biogenic sources of methane
1014 in the Earth's deep subsurface. *Chemical Geology* 226, 328-339.

1015 Sherwood Lollar B., Westgate T. D., Ward J. A., Slater G. F. and Lacrampe-Couloume G. (2002)
1016 Abiogenic formation of alkanes in the Earth's crust as a minor source for global hydrocarbon
1017 reservoirs. *Nature* 416, 522–524.

1018 Sherwood Lollar B., Frape S. K., Weise S. M., Fritz P., Macko S. A. and Welhan J. A. (1993)
1019 Abiogenic methanogenesis in crystalline rocks. *Geochimica Et Cosmochimica Acta* 57, 5087–
1020 5097.

1021 Sleep, N.H. and Zoback, M.D. (2007) Did earthquakes keep the early crust habitable?
1022 *Astrobiology* 7, 1023-1032.

1023 Smith, S.P. (1985) Noble gas solubility in water at high temperature. *Transactions - American*
1024 *Geophysical Union* 66, 397-397.

1025 Smith, S.P. and Kennedy, B.M. (1983) The solubility of noble gases in water and in NaCl brine.
1026 *Geochimica Et Cosmochimica Acta* 47, 503-515.

Stober, I. and Bucher, K. (2007) Hydraulic properties of the crystalline basement. *Hydrogeology Journal* 15, 213-224.

Stober, I. (1997) Permeabilities and Chemical Properties of Water in Crystalline Rocks of the Black Forest, Germany. *Aquatic Geochemistry* 3, 43-60.

Stout, V.L. and Gibbons, M.D. (1955) Gettering of Gas by Titanium. *Journal of Applied Physics* 26, 1488-1492.

Thurston, P., Ayer, J., Goutier, J. and Hamilton, M. (2008) Depositional gaps in Abitibi greenstone belt stratigraphy: a key to exploration for syngenetic mineralization. *Economic Geology* 103, 1097-1134.

Tolstikhin, I.N., Skiba, V.I., Sevost'yanov, A.Y., Kamensky, I.L. and Vetrin, V.R. (2014) Residence sites and origin of noble gases in minerals as exemplified by ilmenite from the alkaline granites of the Kola Peninsula. *Geochemistry International* 52, 1049-1056.

Townend, J. and Zoback, M.D. (2000) How faulting keeps the crust strong. *Geology* 28, 399-402.

Ward, J.A., Slater, G.F., Moser, D.P., Lin, L.H., Lacrampe-Couloume, G., Bonin, A.S., Davidson, M., Hall, J.A., Mislowack, B., Bellamy, R.E.S., Onstott, T.C. and Sherwood Lollar, B. (2004) Microbial hydrocarbon gases in the Witwatersrand Basin, South Africa: Implications for the deep biosphere. *Geochimica Et Cosmochimica Acta* 68, 3239-3250.

Warr, O., Rochelle, C.A., Masters, A. and Ballentine, C.J. (2015) Determining noble gas partitioning within a CO_2–H_2O system at elevated temperatures and pressures. *Geochimica et Cosmochimica* Acta 159, 112-125.

Wetherill, G.W. (1954) Variations in the isotopic abundances of neon and argon extracted from radioactive minerals. *Physical Review* 96, 679-683.

Figures

Figure 1. Location map of Kidd Creek Mine in Timmins and Mines 1 & 2 in the Sudbury Basin.

Latitude & Longitude of each mine are as follows; Kidd Creek Mine: 48° 41' 24" North, 81° 22'

1063 0" West, Mine 1: 46° 39' 25" North, 80° 47' 34" West, Mine 2: 46° 39' 46" North, 81° 20' 34"
1064 West.
1065
1066 **Figure 2.** Average isotopic ratios from each locality relative to ^{36}Ar. The dashed line at 1 is the
1067 isotopic ratio for Air Saturated Water (ASW). ASW ratios given here are derived from seawater
1068 at 10 °C (Kipfer et al., 2002).

1069 **Figure 3.** Comparison of neon isotopic ratios for samples from this and previous study. Data
1070 presented are 2.4 km samples from this work (black squares) and the 2013 study (blue squares),
1071 2.9 km (red circles), Sudbury Mine 1 (green diamonds) and Mine 2 (gold star). Also given is the
1072 Air Saturated Water (ASW) value (orange cross), the mantle (solar) composition (blue cross,
1073 Graham, 2002). The two mixing lines shown for mixing between ASW and typical crustal
1074 radiogenic $^{21}Ne/^{22}Ne$ end-members for the crust (black line - from Ballentine & Burnard, 2002)
1075 and for mixing between ASW and an elevated $^{21}Ne/^{22}Ne$ end-member first defined by the
1076 fracture fluid and fluid inclusion data from the Archean-aged Witwatersrand Basin (red line -
1077 Lippman-Pipke et al., 2011).

1078 **Figure 4.** Xenon excesses over modern air (normalised to ^{130}Xe). For each ^{136}Xe excess the
1079 relative fission spectra for uranium is plotted (dotted lines) which reaches good agreement with
1080 measured excesses for ^{134}Xe, ^{132}Xe and ^{131}Xe. Fission values taken from Ballentine and Burnard,
1081 (2002) and references therein. Fissiogenic excesses were calculated by anchoring the ^{238}U fission
1082 spectra to ^{136}Xe and calculating the expected corresponding $^{131\text{-}134}Xe$ excess.

1083 **Figure 5.** Percentage deviations of $^{124\text{-}129}Xe/^{130}Xe$ in samples compared to modern atmospheric
1084 ratios. Values plotted are averages for each isotope per sampling level at each mine (Table 8).

1085 The average percentage fractionation line for the $^{124\text{-}128}$Xe excesses (dashed lines) was calculated
1086 as follows: 1. All individual percentage excesses for $^{124\text{-}128}$Xe for each sample were divided by
1087 their respective mass difference from ^{130}Xe and an average excess per amu was calculated for
1088 each sample. 2. An average excess per amu was calculated for each sample. Lastly 3. Each
1089 average excess was multiplied by the mass difference from ^{130}Xe and plotted for each isotope. At
1090 Kidd Creek Mine, an additional ^{129}Xe excess is observed as described in Section 5.3, but not
1091 seen in the Sudbury Basin samples.

1092 **Figure 6.** Mean residence time estimates based on radiogenic noble gas accumulation, presented
1093 graphically for all samples and compared to results from Holland et al. (2013). For context the
1094 last known major metasomatic event at Kidd Creek Mine, and the timing of the Sudbury bolide
1095 impact are also provided in the figure (Bleeker and Parrish, 1996; Davis, 2008). Analytical
1096 uncertainties for noble gas analysis are small. The large uncertainties for the error bars in this
1097 figure reflect minimum and maximum estimates in mean residence time estimates based on
1098 uncertainty in bulk porosity estimates for crystalline rock (see text) and are used to provide the
1099 most conservative possible sense of the mean residence time ranges derived from the data.
1100 Where analytical uncertainty exceeds known geological age, the upper limits of uncertainty have
1101 been restricted accordingly.

1102 **Figure 7.** Schematic diagram outlining conceptual model for fractures within crystalline
1103 basement rock.

1104 **Figure 8.** δ^{18}O & δ^{2}H values for fracture fluids at 2.4 km for [1]the original study and [2]resampled
1105 fluids (this work). Values are given in Table 10. All values remain significantly elevated above
1106 the Global Meteoric Water Line with no isotopic evolution over time. This indicates the less old
1107 fluid present in the later samples has undergone a comparable extensive water-rock interaction

and therefore rules out the presence of recent meteoric water. Faded symbols for Kidd Creek Mine 2.9 km & Sudbury are supplementary values from additional sample suites (Frape et al., 1984; Li et al., 2016) which highlight the consistency of the noble gas-associated values with the rest of the ^{2}H & ^{18}O data (with no evidence of their movement towards the GMWL).

Tables

Borehole	Date	Fluid flow (ml/min)	Gas flow (cm^3/min)
Kidd Creek Mine (2.4 km)			
12287	20.09.13	N.M.	variable
12299	03.04.14	180	300
Kidd Creek Mine (2.9 km)			
13684	01.03.12	*	1760
13684	14.06.12	*	1200
BH2	29.11.12	N.M	3600
BH2	16.01.13	N.M.	1000
Sudbury Mine 1 (1.7 km)			
170128	29.11.13	2390	2000
170128	05.03.14	2140	410-1200
170128	22.10.14	2060	170-420
Sudbury Mine 2 (1.4 km)			
47774	06.03.14	2830	1130

Table 1. Locations, dates and flow rates of samples collected from each locality. Dates are presented in DD/MM/YY format. Flowrates given in ml/min and cm^3/min for water and gas respectively. N.M. indicates not measured. * indicates standing water only, no artesian flow. Depth of level below land surface is also provided.

Sample	^{20}Ne	error	^{36}Ar	error	^{84}Kr	error	^{130}Xe	error
Air	1.65E-05		3.14E-05		6.50E-07		3.54E-09	
Kidd Mine								
(2.4 km)								
12287	1.71E-08	0.01E-08	2.22E-07	0.02E-07	5.79E-09	0.07E-09	6.46E-11	0.10E-11
12299	5.40E-08	0.05E-08	3.23E-07	0.03E-07	9.00E-09	0.11E-09	8.85E-11	0.14E-11
Average	**3.55E-08**	**2.61E-08**	**2.73E-07**	**0.71E-07**	**7.4E-09**	**2.27E-09**	**7.66E-11**	**1.69E-11**
Kidd Mine								
(2.9 km)								
13684	6.74E-09	0.06E-09	2.65E-08	0.05E-08	7.09E-10	0.08E-10	8.17E-12	0.12E-12
13684	9.02E-09	0.08E-09	2.28E-08	0.05E-08	7.99E-10	0.10E-10	9.09E-12	0.13E-12
BH2	8.42E-09	0.09E-09	2.66E-08	0.07E-08	8.76E-10	0.11E-10	1.11E-11	0.02E-11
BH2	1.03E-08	0.01E-08	3.07E-08	0.13E-08	9.26E-10	0.11E-10	1.17E-11	0.02E-11
Average	**8.62E-09**	**1.49E-09**	**2.67E-08**	**0.32E-08**	**8.28E-10**	**0.94E-10**	**1.00E-11**	**0.17-11**
Sudbury Mine 1								
(1.7 km)								
170128	7.93E-07	0.08E-07	4.89E-06	0.05E-06	1.41E-07	0.02E-07	1.09E-09	0.02E-09
170128	6.15E-07	0.05E-07	4.12E-06	0.04E-06	1.26E-07	0.02E-07	1.02E-09	0.02E-09
170128	6.59E-07	0.07E-07	6.92E-06	0.07E-06	2.15E-07	0.03E-07	1.75E-09	0.03E-09
Average	**6.89E-07**	**0.93E-07**	**5.31E-06**	**1.45E-06**	**1.61E-07**	**0.48E-08**	**1.29E-09**	**0.40E-09**
Sudbury Mine 2								
(1.4 km)								
47774	3.31E-07	0.03E-07	3.72E-06	0.04E-06	1.11E-07	0.01E-07	1.01E-09	0.02E-09
Average	**3.31E-07**	**0.03E-07**	**3.72E-06**	**0.04E-06**	**1.11E-07**	**0.01E-07**	**1.01E-09**	**0.02E-09**

Table 2. Concentrations of non-radiogenic noble gas isotopes in gas samples. Values given in cm^3 per cm^3 of gas under STP conditions to three significant figures. Isotopes presented here represent non-radiogenic noble gas isotopes which are present in the geological system, that is, atmospheric-derived noble gas naturally occurring in the groundwaters due to water which had equilibrated with atmospheric noble gases at the time of recharge. For each level both individual samples and an average concentration are presented. For each average value the error

1131 incorporates the standard deviation (1 σ) of each individual measurement. Air values (compiled
1132 by (Ozima and Podosek, 2002) have been given for reference.

1133

Sample	^{20}Ne	error	^{36}Ar	error	^{84}Kr	error	^{130}Xe	error
ASW	1.48E-07		1.01E-06		4.00E-08		5.21E-10	
Kidd Mine								
(2.4 km)								
12287	7.74E-08	0.06E-08	1.01E-06	0.01E-06	2.63E-08	0.03E-08	2.93E-10	0.05E-10
12299	1.69E-07	0.02E-07	1.01E-06	0.01E-06	2.81E-08	0.03E-08	2.76E-10	0.04E-10
Average	**1.23E-07**	**0.65E-07**	**1.01E-06**	**0.00E+00**	**2.72E-08**	**0.13E-08**	**2.85E-10**	**0.12E-10**
Kidd Mine								
(2.9 km)								
13684	2.57E-07	0.02E-07	1.01E-06	0.02E-08	2.70E-08	0.03E-08	3.11E-10	0.05E-10
13684	3.99E-07	0.03E-07	1.01E-06	0.02E-08	3.54E-08	0.04E-08	4.03E-10	0.06E-10
BH2	3.19E-07	0.04E-07	1.01E-06	0.02E-08	3.32E-08	0.04E-08	4.19E-10	0.06E-10
BH2	3.39E-07	0.03E-07	1.01E-06	0.04E-08	3.04E-08	0.04E-08	3.85E-10	0.06E-10
Average	**3.29E-07**	**0.59E-07**	**1.01E-06**	**0.00E+00**	**3.15E-08**	**0.36E-08**	**3.79E-10**	**0.48E-10**
Sudbury Mine 1								
(1.7 km)								
170128	1.64E-07	0.02E-07	1.01E-06	0.01E-06	2.92E-08	0.04E-08	2.26E-10	0.04E-10
170128	1.51E-07	0.01E-07	1.01E-06	0.01E-06	3.08E-08	0.04E-08	2.49E-10	0.04E-10
170128	9.61E-08	0.10E-08	1.01E-06	0.01E-06	3.13E-08	0.04E-08	2.55E-10	0.04E-10
Average	**1.37E-07**	**0.39E-07**	**1.01E-06**	**0.00E+00**	**3.04E-08**	**0.11E-08**	**2.43E-10**	**0.15E-10**
Sudbury Mine 2								
(1.4 km)								
47774	8.98E-08	0.08E-08	1.01E-06	0.01E-06	3.00E-08	0.04E-08	2.75E-10	0.04E-10
Average	**8.98E-08**	**0.08E-08**	**1.01E-06**	**0.00E+00**	**3.00E-08**	**0.04E-08**	**2.75E-10**	**0.04E-10**

1134

1135 Table 3. Concentrations of non-radiogenic noble gas isotopes expressed per cm^3 of fracture fluid
1136 to three significant figures. Concentrations are calculated by dividing the concentration per cm^3
1137 of gas by the total amount of water which has been degassed. Degassed water volume is derived

1138 assuming a ^{36}Ar content of 1.01×10^{-6} cm^3/cm^3 of water based on concentrations in seawater at
1139 10°C after the methods of (Kipfer et al., 2002). For each level both individual samples and an
1140 average concentration is presented. The error on the average value incorporates the standard
1141 deviation (1 σ). Air Saturated seawater at 10°C are provided for reference (Kipfer et al., 2002) .

Sample	$^{3}He/^{4}He$ (R/R_A)	error	$^{20}Ne/^{22}Ne$	error	$^{21}Ne/^{22}Ne$	error	$^{40}Ar/^{36}Ar$	error	$^{38}Ar/^{36}Ar$	error
Air/ASW	1.0000		9.80		0.029		295.5		1.880E-01	
Kidd Mine (2.4 km)										
12287	2.30E-02	0.07E-02	8.64	0.02	2.861E-01	0.002 E-01	16300	100	1.94E-01	0.02
12299	2.14E-02	0.05E-02	8.770	0.004	2.397E-01	0.001 E-01	13800	100	1.93E-01	0.02
Average	**2.22E-02**	**0.11E-02**	**8.71**	**0.09**	**2.63E-01**	**0.33** E-01	**15100**	**1780**	**1.94E-01**	**0.01**
Kidd Mine (2.9 km)										
13684	2.56E-02	0.06E-02	5.06	0.01	5.935E-01	0.002E-01	77500	1270	2.25E-01	0.05E-01
13684	2.47E-02	0.06E-02	5.27	0.02	5.722E-01	0.003E-01	91000	1990	1.99E-01	0.09E-01
BH2	2.59E-02	0.05E-02	5.324	0.004	6.189E-01	0.002E-01	116000	2680	2.28E-01	0.07E-01
BH2	2.61E-02	0.05E-02	5.44	0.01	6.056E-01	0.005E-01	125000	5230	1.83E-01	0.12E-01
Average	**2.56E-02**	**0.06E-02**	**5.27**	**0.16**	**5.98E-01**	**0.20E-01**	**102000**	**22000**	**2.09E-01**	**0.22E-01**
Sudbury Mine 1 (1.7 km)										
170128	1.96E-02	0.04E-02	8.728	0.004	1.38E-01	0.001E-01	4330	5	1.912E-01	0.005E-01
170128	1.95E-02	0.04E-02	8.772	0.004	1.39E-01	0.001E-01	4430	6	1.954E-01	0.004E-01
170128	1.95E-02	0.04E-02	8.88	0.01	1.37E-01	0.001E-01	4310	4	1.918E-01	0.005E-01
Average	**1.95E-02**	**0.01E-02**	**8.79**	**0.08**	**1.38E-01**	**0.01E-01**	**4350**	**63**	**1.93E-01**	**0.02E-01**
Sudbury Mine 2 (1.4 km)										
47774	2.30E-02	0.0005	7.960	0.002	1.324E-01	0.001E-01	17600	82	1.97E-01	0.01E-01
Average	**2.30E-2**	**0.001**	**7.960**	**0.002**	**1.324E-01**	**0.001E-01**	**17600**	**82**	**1.97E-01**	**0.01E-01**

Table 4. Noble gas isotope ratios for the sample suite given to three significant figures. Where the uncertainty is lower than the third significant figure an additional significant figure is given. For each level both individual samples and an average concentration is presented. The error on the average value is taken as the standard deviation (1 σ). Helium $^{3}He/^{4}He$ ratios are given in R/R_A where $R_{A(air)} = 1$. Absolute $^{3}He/^{4}He_{(air)} = 1.399 \times 10^{-6}$ (Mamyrin et al., 1970). Air/ASW values (compiled by (Ozima and Podosek, 2002) have been given for reference.

Sample	$^{124}Xe/^{130}Xe$	error	$^{126}Xe/^{130}Xe$	error	$^{128}Xe/^{130}Xe$	error	$^{129}Xe/^{130}Xe$	error
Air/ASW	2.34E-02		2.18E-02		4.72E-01		6.496	
Kidd Mine (2.4 km)								
12287	2.37E-02	0.01E-02	2.18 E-02	0.01E-02	4.79E-01	0.02E-01	6.56	0.03
12299	2.37E-02	0.02E-02	2.18 E-02	0.02E-02	4.74E-01	0.04E-01	6.61	0.04
Average	**2.370E-02**	**0.003E-02**	**2.183** E-02	**0.001E-02**	**4.76E-01**	**0.03E-01**	**6.58**	**0.03**
Kidd Mine (2.9 km)								
13684	2.40E-02	0.01E-02	2.19 E-02	0.01E-02	4.82E-01	0.02E-01	6.72	0.02
13684	2.39E-02	0.01E-02	2.20 E-02	0.01E-02	4.78E-01	0.02E-01	6.71	0.01
BH2	2.42E-02	0.02E-02	2.23 E-02	0.01E-02	4.86E-01	0.02E-01	6.80	0.02
BH2	2.41E-02	0.01E-02	2.23 E-02	0.01E-02	4.83E-01	0.02E-01	6.75	0.01
Average	**2.41E-02**	**0.01E-02**	**2.21** E-02	**0.02E-02**	**4.82E-01**	**0.03E-01**	**6.75**	**0.04**
Sudbury Mine 1 (1.7 km)								
170128	2.37E-02	0.01E-02	2.19 E-02	0.01E-02	4.74E-01	0.02E-01	6.52	0.03
170128	2.37E-02	0.01E-02	2.19 E-02	0.01E-02	4.75E-01	0.02E-01	6.53	0.03
170128	2.35E-02	0.01E-02	2.21 E-02	0.01E-02	4.76E-01	0.02E-01	6.51	0.03
Average	**2.36E-02**	**0.01E-02**	**2.20** E-02	**0.01E-02**	**4.75E-01**	**0.01E-01**	**6.52**	**0.01**
Sudbury Mine 2 (1.4 km)								
47774	2.34E-02	0.01E-02	2.21 E-02	0.01E-02	4.77E-01	0.03E-01	6.55	0.03
Average	**2.**34E-02	**0.01E-02**	**2.21** E-02	**0.01E-02**	**4.77E-01**	**0.03E-01**	**6.55**	**0.03**

Sample	$^{131}Xe/^{130}Xe$	error	$^{132}Xe/^{130}Xe$	error	$^{134}Xe/^{130}Xe$	error	$^{136}Xe/^{130}Xe$	error
Air/ASW	5.213		6.607		2.563		2.176	
Kidd Mine (2.4 km)								
12287	5.22	0.03	6.72	0.03	2.77	0.01	2.41	0.01
12299	5.45	0.03	6.78	0.04	2.80	0.02	2.44	0.01
Average	**5.33**	**0.16**	**6.75**	**0.04**	**2.79**	**0.02**	**2.42**	**0.02**
Kidd Mine (2.9 km)								
13684	5.33	0.01	7.60	0.02	4.16	0.02	4.11	0.02
13684	5.94	0.02	7.51	0.02	4.03	0.01	3.94	0.01
BH2	5.35	0.01	7.66	0.02	4.24	0.01	4.21	0.02
BH2	5.31	0.01	7.53	0.02	4.09	0.01	4.01	0.01
Average	**5.48**	**0.30**	**7.58**	**0.07**	**4.13**	**0.09**	**4.07**	**0.12**
Sudbury Mine 1 (1.7 km)								
170128	5.22	0.02	6.72	0.03	2.75	0.01	2.39	0.01
170128	5.23	0.02	6.74	0.03	2.76	0.01	2.40	0.01
170128	5.21	0.02	6.71	0.03	2.74	0.01	2.37	0.01
Average	**5.22**	**0.01**	**6.72**	**0.02**	**2.75**	**0.01**	**2.39**	**0.01**
Sudbury Mine 2 (1.4 km)								
47774	5.27	0.03	7.08	0.04	3.27	0.02	3.00	0.02
Average	**5.27**	**0.03**	**7.08**	**0.04**	**3.27**	**0.02**	**3.00**	**0.02**

1156 Table 5. Xenon noble gas isotope ratios for the sample suite given to three significant figures.
1157 Where the uncertainty is lower than the third significant figure an additional significant figure is
1158 given. For each level both individual samples and an average concentration is presented. The
1159 error on the average value incorporates the standard deviation (1 σ). Air values (compiled by
1160 (Ozima and Podosek, 2002) have been given for reference.

1161

Sample	^{4}He*	error	^{21}Ne*	error	^{40}Ar*	error	^{136}Xe*	error
Kidd Mine								
(2.4 km)								
12287	6.88E-02	0.10E-02	2.33E-09	0.03E-09	1.62E-02	0.02E-02	6.87E-11	0.15E-11
12299	9.49E-02	0.13E-02	4.11E-09	0.05E-09	1.36E-02	0.02E-02	7.27E-11	0.17E-11
Average	**8.19E-02**	**1.85E-02**	**3.22E-09**	**1.26E-09**	**1.49E-02**	**0.18E-02**	**7.07E-11**	**0.28E-11**
Kidd Mine								
(2.9 km)								
13684	6.69E-01	0.09E-01	2.93E-08	0.04E-08	7.79E-02	0.16E-02	6.02E-10	0.13E-10
13684	8.65E-01	0.12E-01	4.22E-08	0.05E-08	9.15E-02	0.22E-02	7.11E-10	0.15E-10
BH2	9.09E-01	0.13E-01	3.61E-08	0.06E-08	1.17E-01	0.03E-01	8.51E-10	0.18E-10
BH2	7.47E-01	0.11E-01	3.67E-08	0.04E-08	1.26E-01	0.05E-01	7.06E-10	0.15E-10
Average	**7.97E-01**	**1.10E-01**	**3.61E-08**	**5.29E-09**	**1.03E-01**	**2.22E-02**	**7.17E-10**	**1.03E-10**
Sudbury Mine 1								
(1.7 km)								
170128	6.96E-02	0.10E-02	2.11E-09	0.03E-09	4.07E-03	0.05E-03	4.81E-11	0.11E-11
170128	5.88E-02	0.09E-02	1.93E-09	0.02E-09	4.17E-03	0.05E-03	5.48E-11	0.12E-11
170128	3.95E-02	0.06E-02	1.20E-09	0.02E-09	4.05E-03	0.06E-03	5.07E-11	0.12E-11
Average	**5.60E-02**	**1.53E-02**	**1.75E-09**	**0.48E-09**	**4.09E-03**	**0.06E-03**	**5.12E-11**	**0.34E-11**
Sudbury Mine 2								
(1.4 km)								
47774	2.79E-02	0.04E-02	1.23E-09	0.02E-11	1.75E-02	0.02E-02	2.27E-10	0.05E-10
Average	**2.79E-02**	**0.04E-02**	**1.23E-09**	**0.02E-11**	**1.75E-02**	**0.02E-02**	**2.27E-10**	**0.05E-10**

1162

1163 Table 6. Concentrations of excess radiogenic noble gas isotopes expressed per cm^3 of fracture
1164 fluid given to three significant figures. The method for deriving concentrations within the
1165 fracture fluid is outlined in the main text. Isotopes presented here represent radiogenic noble gas
1166 isotopes which have accumulated within the system over time due to naturally occurring
1167 radioactive decay of parent isotopes. *In situ* radiogenic noble gas concentrations are derived by
1168 multiplying the measured ratios (Tables 5 & 6) by non-radiogenic concentrations (Table 3) and
1169 subtracting this from total concentrations of the radiogenic isotopes. For each level both
1170 individual samples and an average concentration is presented. The error on the average value
1171 incorporates the standard deviation (1 σ).

1172

Sample	^{4}He*	error	^{21}Ne*	error	^{40}Ar*	error	^{136}Xe*	error
Kidd Mine								
(2.9 km)								
13684	3.84E-01	0.05E-01	1.69E-08	0.02E-08	7.79E-02	0.16E-02	1.01E-09	0.02E-09
13684	3.19E-01	0.05E-01	1.56E-08	0.02E-08	9.15E-02	0.23E-02	9.20E-10	0.19E-10
BH2	4.21E-01	0.06E-01	1.67E-08	0.03E-08	1.17E-01	0.30E-02	1.06E-09	0.02E-09
BH2	3.25E-01	0.05E-01	1.60E-08	0.02E-08	1.26E-01	0.55E-02	9.55E-10	0.20E-10
Average	**3.58E-01**	**0.49E-01**	**1.62E-08**	**0.237E-08**	**1.03E-01**	**0.22E-01**	**9.85E-10**	**1.41E-10**

1173

1174 Table 7. Corrected concentrations of excess radiogenic noble gas isotopes per cm^3 of fracture
1175 fluid for Kidd Creek Mine at 2.9 km depth given to three significant figures. Excesses corrected
1176 for effect of Rayleigh degassing using ASW-derived component (see text).

1177

1178

Sample	^{124}Xe (%)	error	^{126}Xe (%)	error	^{128}Xe (%)	error	^{129}Xe (%)	error
Kidd Mine								
(2.4 km)								
12287	1.51	0.01	0.165	0.001	1.50	0.01	0.96	0.01
12299	1.30	0.01	0.115	0.001	0.535	0.004	1.72	0.01
Average	**1.40**	**0.14**	**0.140**	**0.036**	**1.02**	**0.68**	**1.34**	**0.54**
Kidd Mine								
(2.9 km)								
13684	2.73	0.02	0.616	0.003	2.23	0.01	3.48	0.01
13684	2.39	0.01	1.05	0.01	1.33	0.01	3.36	0.01
BH2	3.39	0.02	2.12	0.01	2.97	0.02	4.64	0.01
BH2	3.30	0.02	2.39	0.01	2.44	0.01	3.91	0.01
Average	**2.95**	**0.48**	**1.54**	**0.85**	**2.24**	**0.68**	**3.85**	**0.58**
Sudbury Mine								
1 (1.7 km)								
170128	1.62	0.01	0.563	0.003	0.613	0.003	0.315	0.001
170128	1.34	0.01	0.536	0.003	0.626	0.002	0.537	0.002
170128	0.51	0.003	1.22	0.01	0.887	0.004	0.204	0.001
Average	**1.16**	**0.57**	**0.772**	**0.386**	**0.709**	**0.154**	**0.352**	**0.170**
Sudbury Mine								
2 (1.4 km)								
47774	0.036	0.0002	1.45	0.01	1.09	0.01	0.768	0.004

Table 8. Percentage deviations of $^{124\text{-}129}$Xe/^{130}Xe in samples over modern atmospheric ratios given to three significant figures. Where the uncertainty is lower than the third significant figure an additional significant figure is given. Average values and the standard deviation are also provided.

Sample location	^{4}He Age	±	^{21}Ne Age	±	^{40}Ar Age	±	^{136}Xe Age	±	Ave	±
12261	850	386	1340	609	971	439	1509	686	1168	309
12299-1	1493	678	1527	697	1396	632	1666	757	1521	112
12299-2	951	432	1594	728	999	453	1321	601	1216	301
12299-3	1142	515	1570	720	1095	496	1613	731	1355	274
12287-2	666	303	1174	538	884	400	919	418	911	208
Kidd Mine (2.4 km)[1]	**1026**	**577**	**1443**	**683**	**1078**	**559**	**1411**	**719**	**1240**	**218**
12287	482	219	166	75	638	288	149	68	359	241
12299	658	298	290	132	552	249	157	71	414	231
Kidd Mine (2.4 km)[2]	**570**	**289**	**228**	**136**	**595**	**278**	**153**	**70**	**387**	**229**
13684	2149	975	1024	464	1884	850	1763	800	1705	482
13684	1834	832	951	431	2078	938	1627	738	1622	484
BH2	2316	1050	1015	460	2387	1077	1842	836	1890	632
BH2	1860	844	973	441	2493	1129	1683	764	1752	625
Kidd Mine (2.9 km)	**2023**	**959**	**986**	**470**	**2226**	**1112**	**1729**	**822**	**1741**	**543**
170128	790	389	245	121	224	101	171	84	357	290
170128	671	331	225	111	229	103	194	96	330	228
170128	456	225	140	69	222	100	180	89	250	142
Sudbury Mine 1 (1.7 km)	**640**	**360**	**204**	**115**	**225**	**101**	**182**	**90**	**313**	**219**
47774	344	170	153	75	850	383	828	408	544	350
Sudbury Mine 2 (1.4 km)	**344**	**170**	**153**	**75**	**850**	**383**	**828**	**408**	**544**	**350**

Table 9. Individual borehole and overall average ages for each sampling locality for each radiogenic isotope based on radiogenic excesses. Ages given in Ma. [1]Represents the age of Kidd Mine at 2.4 km depth recalculated from Holland et al. (2013) using new estimates of bulk porosity as a function of depth and renormalizing to ^{36}Ar (Sherwood Lollar et al., 2014). [2]Represents ages derived from samples taken from the same boreholes as the Holland et al. (2013) study 44 months later. Residence times are calculated from the average radiogenic excess per sample location (Tables 4 and 7). The observed uncertainty is primarily a result of poor constraints on the bulk porosity (± 45 %) rather than analytical uncertainty (1-2 %).

Sample location	$\delta^{18}O$	error	$\delta^{2}H$	error
12261	-12.8	0.2	-32.0	0.8
12299-1	-12.8	0.2	-38.6	0.8
12299-2	-13.3	0.2	-35.8	0.8
12299-3	-13.5	0.2	-36.7	0.8
12287-2	-13.0	0.2	-40.5	0.8
Kidd Mine (2.4 km)[1]	**-13.1**	**0.3**	**-36.7**	**3.2**
12287	-13.1	0.2	-35.3	0.8
12299	-12.9	0.2	-33.1	0.8
Kidd Mine (2.4 km)[2]	**-13.0**	**0.2**	**-34.2**	**1.6**

Table 10. $\delta^{18}O$ & $\delta^{2}H$ values for fracture fluids at 2.4 km for [1]the original study and [2]resampled fluids (this work). Values are expressed as per mil (‰) variations from Vienna Standard Mean Ocean Water (VSMOW). Errors for individual measurements are ±0.2 and ±0.8 ‰ for $\delta^{18}O$ and $\delta^{2}H$ respectively. Analytical techniques are outlined in Appendix B.

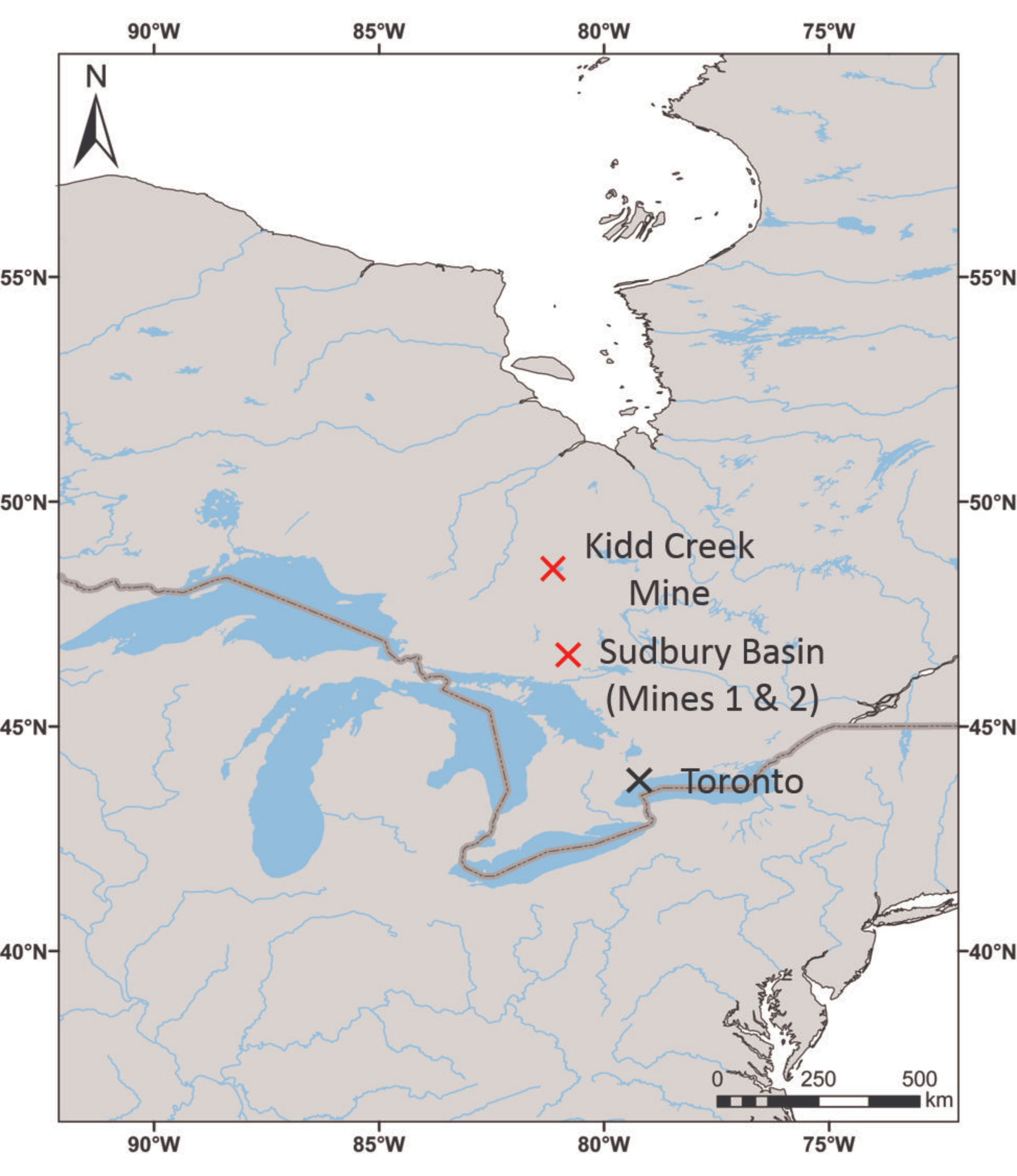
90°W
85°W
80°W
75°W
N
55°N
50°N
45°N
40°N
Kidd Creek
Mine
Sudbury Basin
(Mines 1 & 2)
Toronto
0
250
500
km

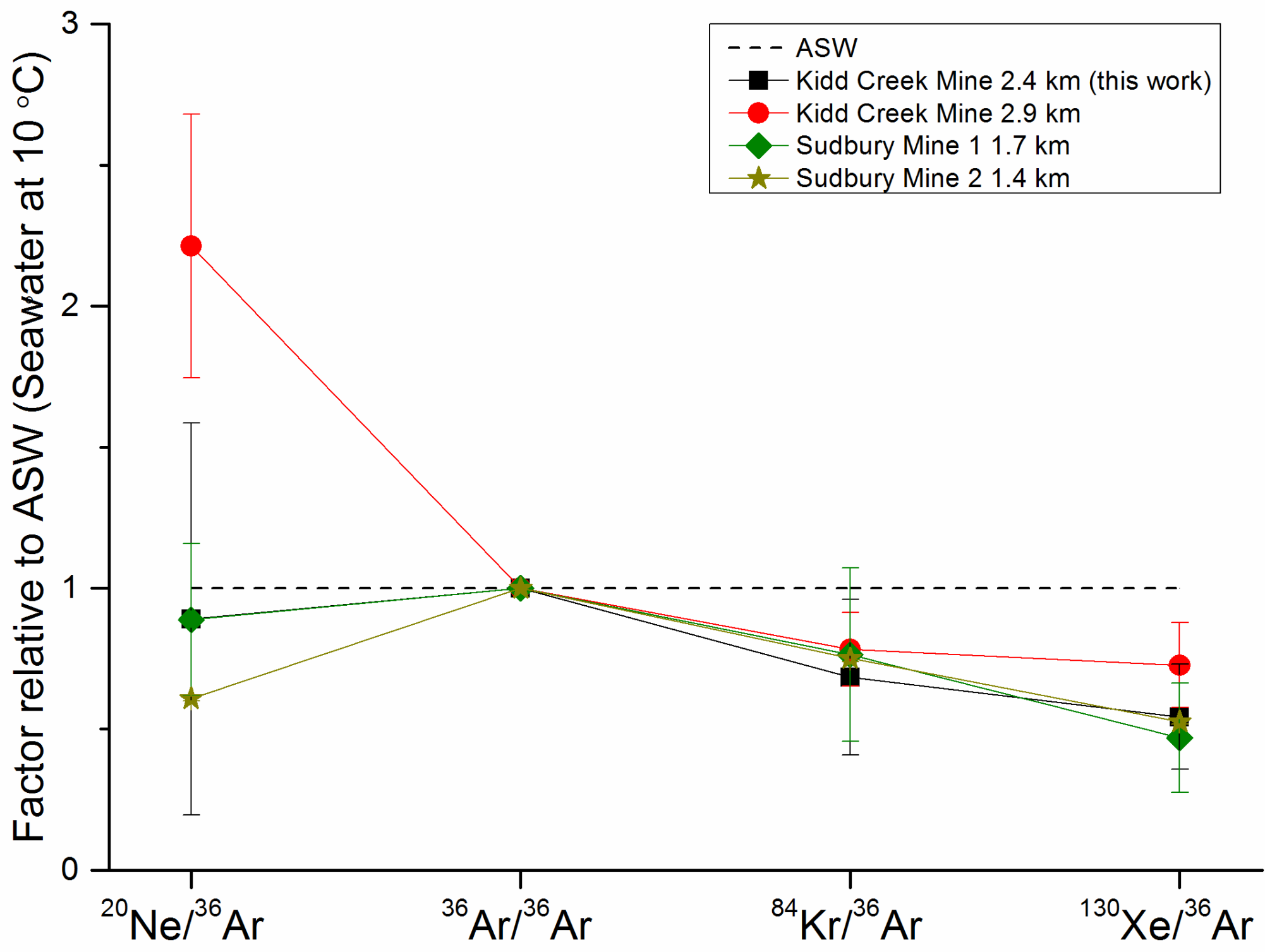
ASW
Kidd Creek Mine 2.4 km (this work)
Kidd Creek Mine 2.9 km
Sudbury Mine 1 1.7 km
Sudbury Mine 2 1.4 km
Factor relative to ASW (Seawater at 10 °C)
3
2
1
0
20Ne/36Ar
36Ar/36Ar
84Kr/36Ar
130Xe/36Ar

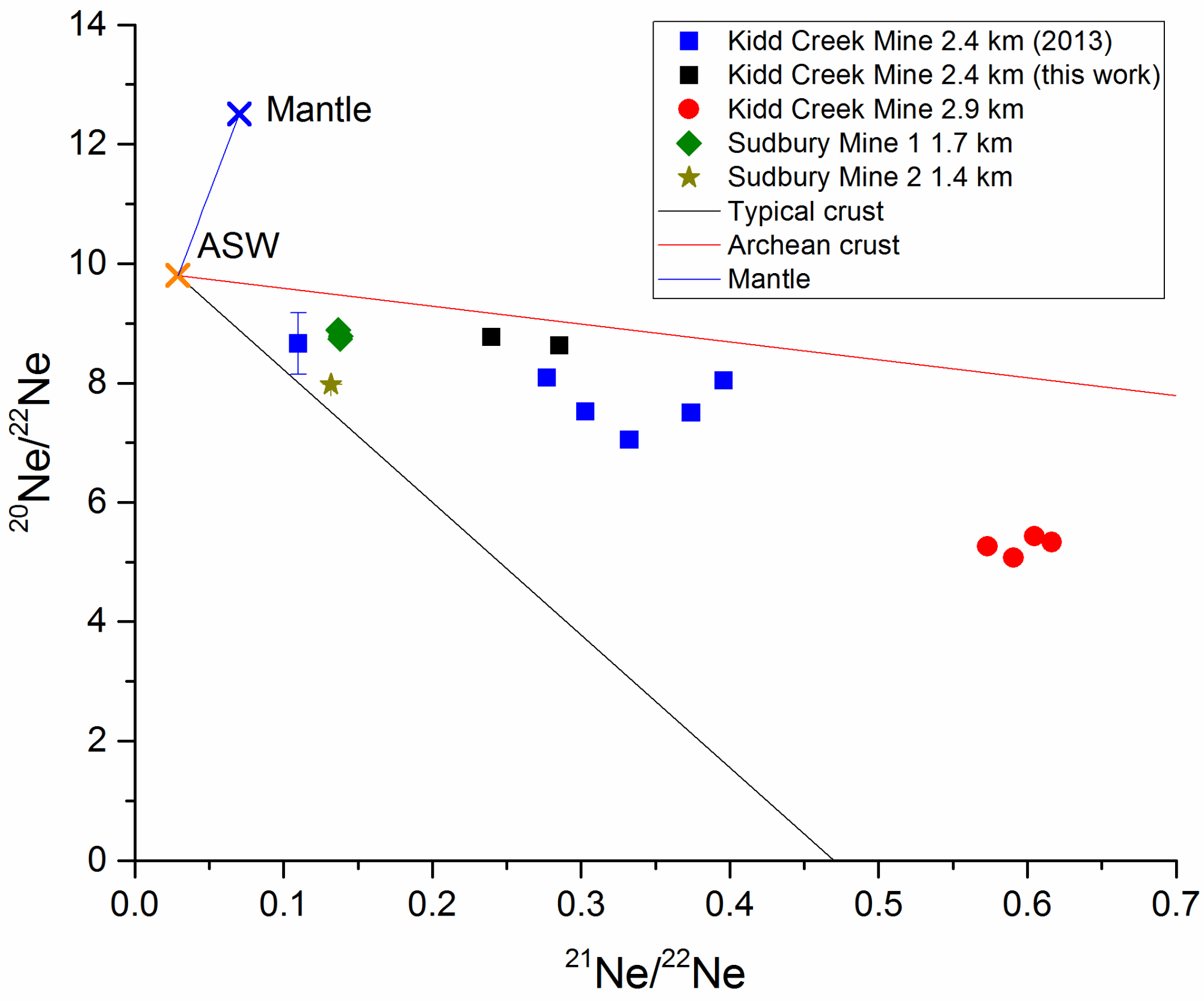
Kidd Creek Mine 2.4 km (2013)
Kidd Creek Mine 2.4 km (this work)
Kidd Creek Mine 2.9 km
Sudbury Mine 1 1.7 km
Sudbury Mine 2 1.4 km
Typical crust
Archean crust
Mantle
Mantle
ASW
$^{20}Ne/^{22}Ne$
$^{21}Ne/^{22}Ne$
0
2
4
6
8
10
12
14
0.0
0.1
0.2
0.3
0.4
0.5
0.6
0.7

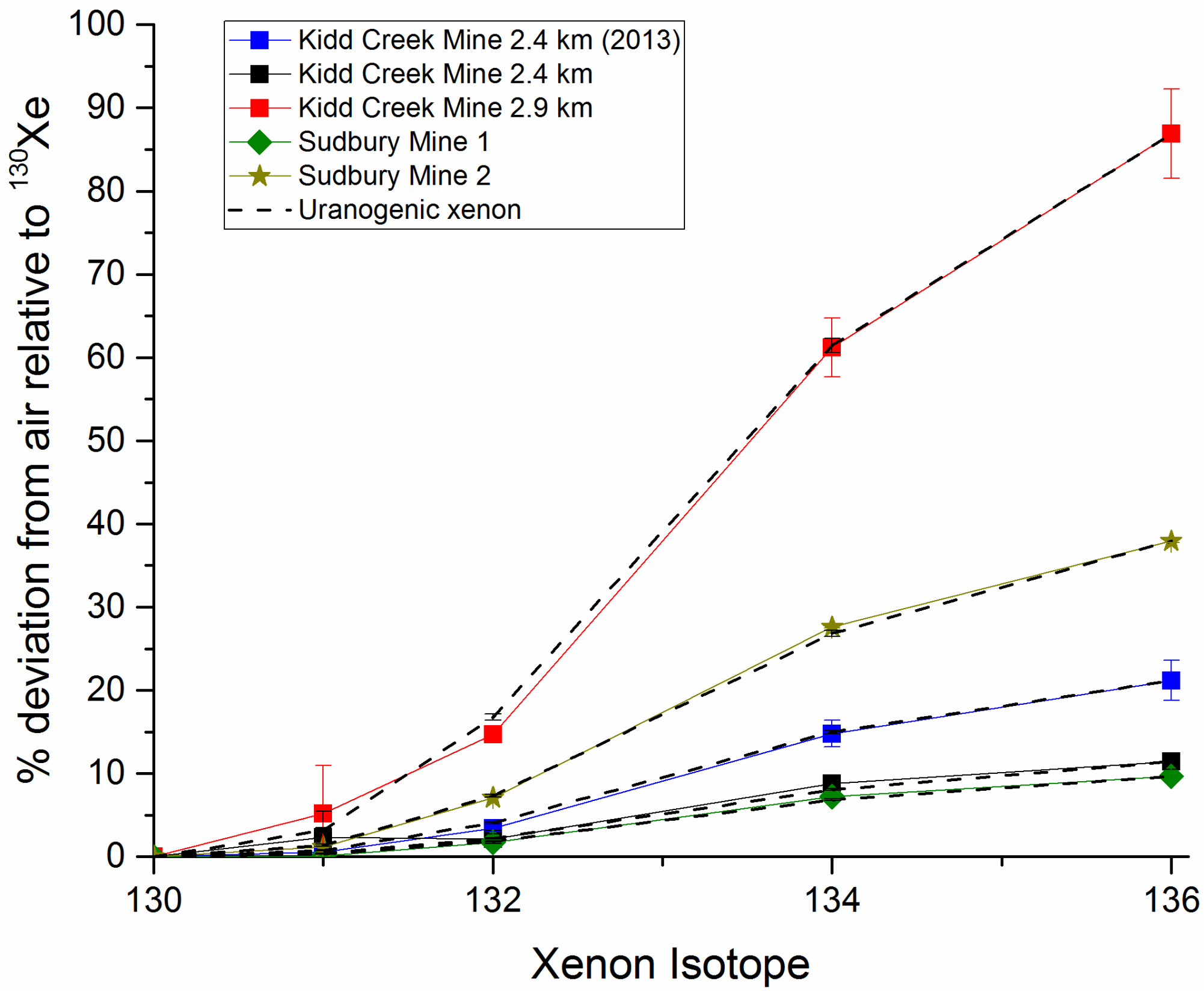
Kidd Creek Mine 2.4 km (2013)
Kidd Creek Mine 2.4 km
Kidd Creek Mine 2.9 km
Sudbury Mine 1
Sudbury Mine 2
Uranogenic xenon
% deviation from air relative to ^{130}Xe
Xenon Isotope
0
10
20
30
40
50
60
70
80
90
100
130
132
134
136

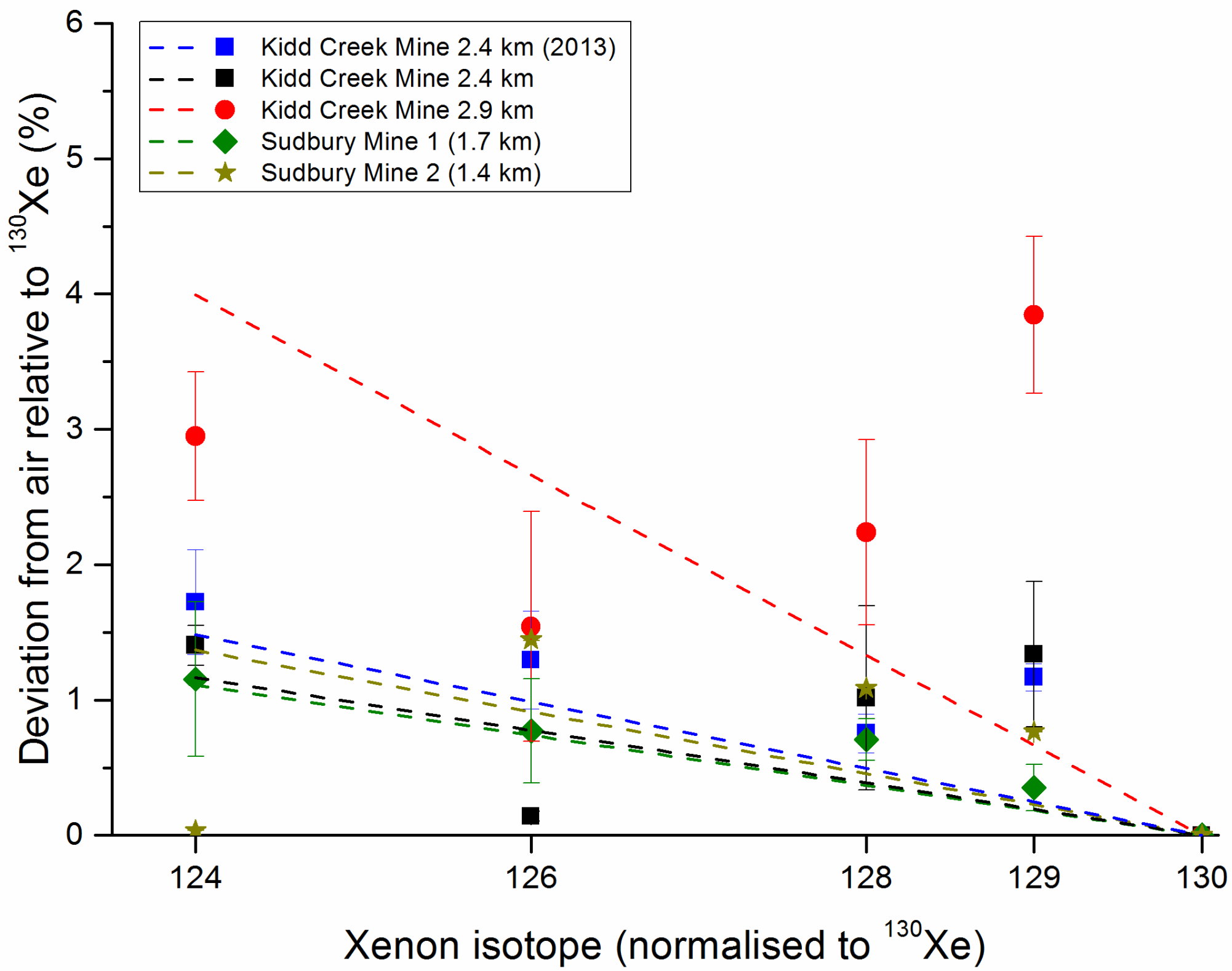
Kidd Creek Mine 2.4 km (2013)
Kidd Creek Mine 2.4 km
Kidd Creek Mine 2.9 km
Sudbury Mine 1 (1.7 km)
Sudbury Mine 2 (1.4 km)
Deviation from air relative to ^{130}Xe (%)
0
1
2
3
4
5
6
124
126
128
129
130
Xenon isotope (normalised to ^{130}Xe)

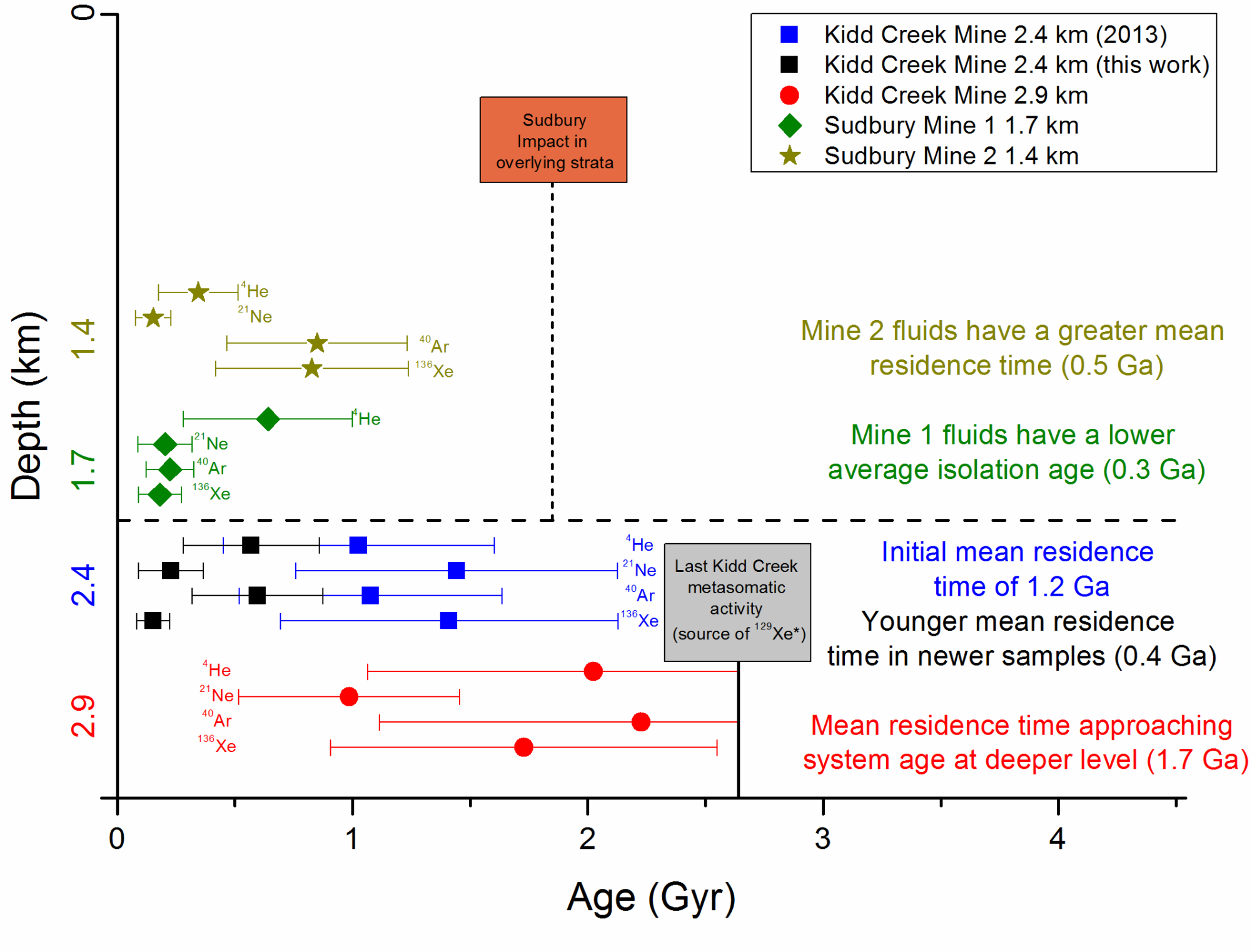
Kidd Creek Mine 2.4 km (2013)
Kidd Creek Mine 2.4 km (this work)
Kidd Creek Mine 2.9 km
Sudbury Mine 1 1.7 km
Sudbury Mine 2 1.4 km
Sudbury Impact in overlying strata
Depth (km)
0
1.4
1.7
2.4
2.9
^{4}He
^{21}Ne
^{40}Ar
^{136}Xe
Last Kidd Creek metasomatic activity (source of ^{129}Xe*)
Mine 2 fluids have a greater mean residence time (0.5 Ga)
Mine 1 fluids have a lower average isolation age (0.3 Ga)
Initial mean residence time of 1.2 Ga
Younger mean residence time in newer samples (0.4 Ga)
Mean residence time approaching system age at deeper level (1.7 Ga)
0
1
2
3
4
Age (Gyr)

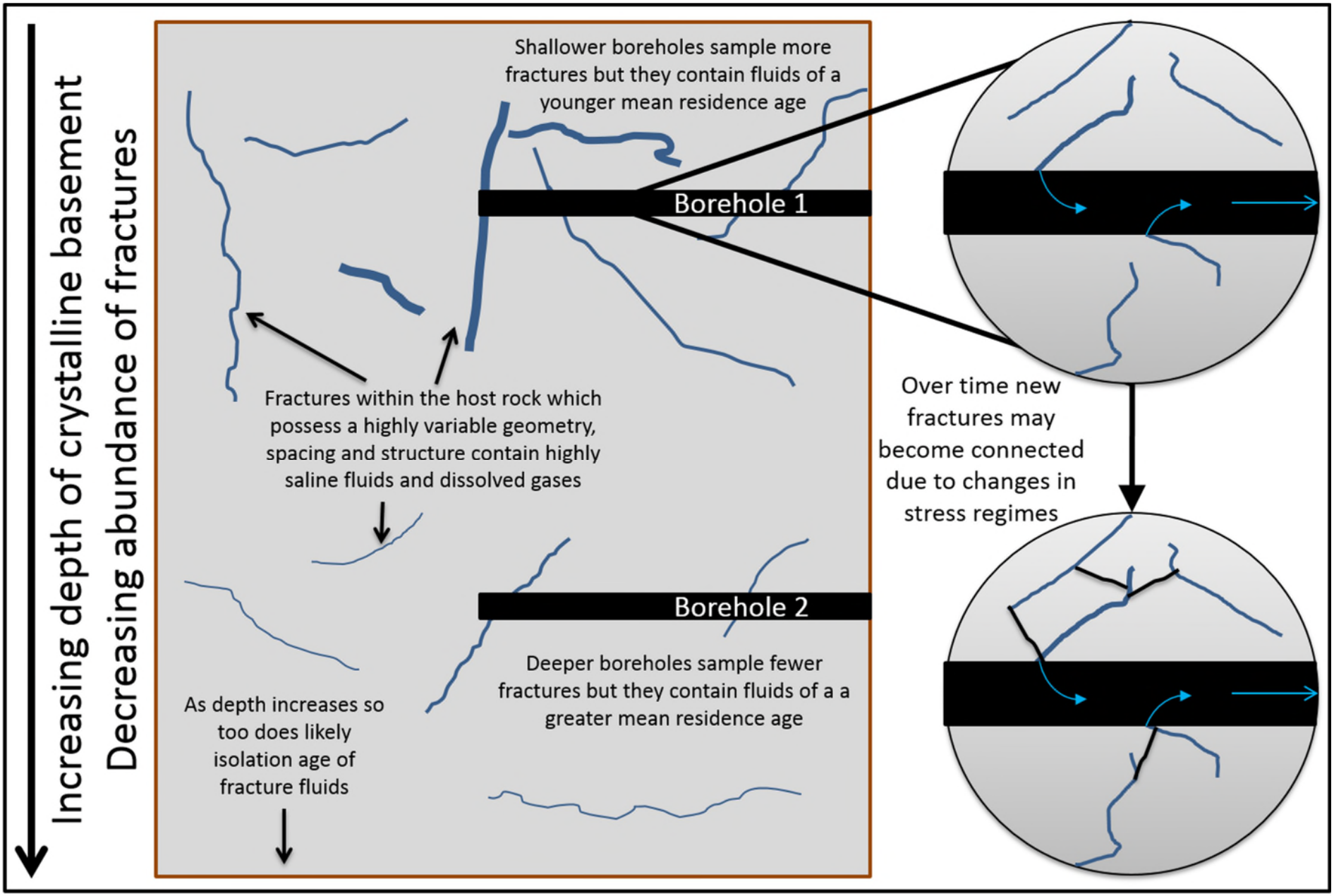
Increasing depth of crystalline basement
Decreasing abundance of fractures
Shallower boreholes sample more fractures but they contain fluids of a younger mean residence age
Borehole 1
Fractures within the host rock which possess a highly variable geometry, spacing and structure contain highly saline fluids and dissolved gases
Over time new fractures may become connected due to changes in stress regimes
Borehole 2
Deeper boreholes sample fewer fractures but they contain fluids of a a greater mean residence age
As depth increases so too does likely isolation age of fracture fluids

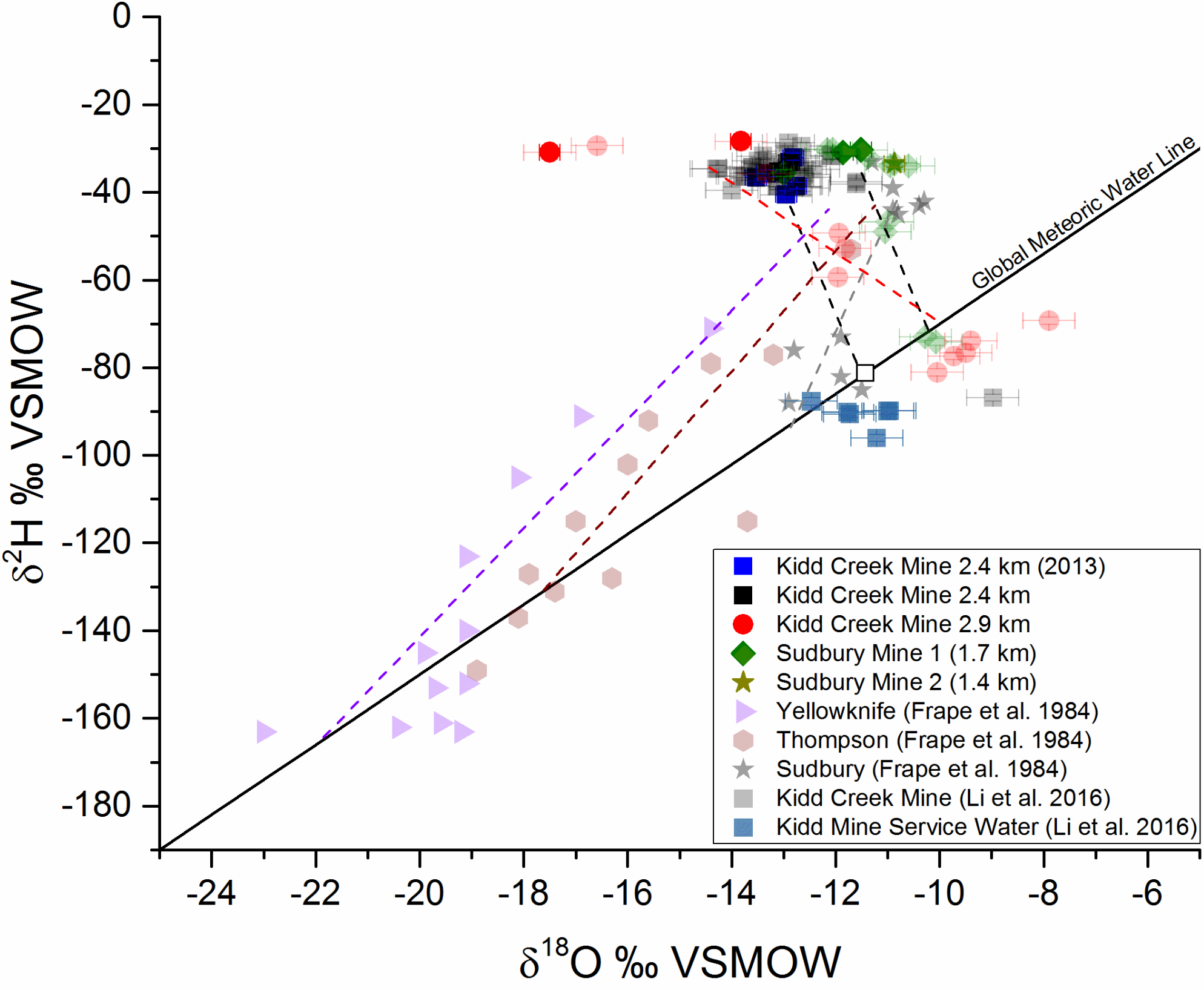
0
-20
-40
-60
-80
-100
-120
-140
-160
-180
δ2H ‰ VSMOW
-24
-22
-20
-18
-16
-14
-12
-10
-8
-6
δ18O ‰ VSMOW
Global Meteoric Water Line
Kidd Creek Mine 2.4 km (2013)
Kidd Creek Mine 2.4 km
Kidd Creek Mine 2.9 km
Sudbury Mine 1 (1.7 km)
Sudbury Mine 2 (1.4 km)
Yellowknife (Frape et al. 1984)
Thompson (Frape et al. 1984)
Sudbury (Frape et al. 1984)
Kidd Creek Mine (Li et al. 2016)
Kidd Mine Service Water (Li et al. 2016)

Appendix A: Concentrations and ratios within gas samples

Sample	^{3}He	Err	^{4}He	Err	^{20}Ne	Err	^{21}Ne	Err	^{21}Ne*	Err	^{22}Ne	Err
Kidd Mine (2.4 km)												
12287	4.89E-10	0.17E-10	1.52E-02	0.02E-02	1.71E-08	0.01E-08	5.65E-10	0.05E-10	5.14E-10	0.06E-10	1.97E-09	0.02E-09
12299	9.11E-10	0.26E-10	3.04E-02	0.04E-02	5.40E-08	0.05E-08	1.48E-09	0.01E-09	1.32E-09	0.02E-09	6.15E-09	0.06E-09
Average	**7.00E-10**	**2.99E-10**	**2.28E-02**	**1.08E-02**	**3.55E-08**	**2.61E-08**	**1.02E-09**	**0.644E-09**	**9.15E-10**	**0.56E-10**	**4.06E-09**	**2.96E-09**
Kidd Mine (2.9 km)												
13684	6.28E-10	0.17E-10	1.76E-02	0.02E-02	6.74E-09	0.06E-09	7.90E-10	0.07E-10	7.70E-10	0.09E-10	1.33E-09	0.01E-09
13684	6.76E-10	0.19E-10	1.95E-02	0.03E-02	9.02E-09	0.08E-09	9.80E-10	0.09E-10	9.54E-10	0.12E-10	1.71E-09	0.02E-09
BH2	8.68E-10	0.22E-10	2.40E-02	0.03E-02	8.42E-09	0.09E-09	9.78E-10	0.11E-10	9.53E-10	0.15E-10	1.58E-09	0.02E-09
BH2	8.30E-10	0.22E-10	2.27E-02	0.03E-02	1.03E-08	0.01E-08	1.15E-09	0.01E-09	1.12E-09	0.01E-09	1.90E-09	0.02E-09
Average	**7.50E-10**	**1.17E-10**	**2.10E-02**	**0.29E-02**	**8.62E-09**	**1.49E-09**	**9.75E-10**	**1.47E-10**	**9.49E-10**	**1.42E-10**	**1.63E-09**	**0.24E-09**
Sudbury Mine 1 (1.7 km)												
170128	9.25E-09	0.25E-09	3.37E-01	0.05E-01	7.93E-07	0.08E-07	1.26E-08	0.01E-08	1.02E-08	0.01E-08	9.09E-08	0.09E-08
170128	6.55E-09	0.18E-09	2.40E-01	0.04E-01	6.15E-07	0.06E-07	9.72E-09	0.09E-09	7.90E-09	0.10E-09	7.02E-08	0.06E-08
170128	7.39E-09	0.21E-09	2.71E-01	0.04E-01	6.59E-07	0.07E-07	1.02E-08	0.01E-08	8.23E-09	0.12E-09	7.42E-08	0.08E-08
Average	**7.73E-09**	**1.38E-09**	**2.83E-01**	**0.50E-01**	**6.89E-07**	**0.93E-07**	**1.08E-08**	**0.15E-08**	**8.78E-09**	**1.25E-09**	**7.84E-08**	**1.10E-08**
Sudbury Mine 2 (1.4 km)												
47774	3.30E-09	0.09E-09	1.03E-01	0.01E-01	3.31E-07	0.03E-07	5.51E-09	0.05E-09	4.53E-09	0.06E-09	4.16E-08	0.04E-08
Average	**3.30E-09**	**0.09E-09**	**1.03E-01**	**0.01E-01**	**3.31E-07**	**0.03E-07**	**5.51E-09**	**0.05E-09**	**4.53E-09**	**0.06E-09**	**4.16E-08**	**0.04E-08**

Table A1. Concentrations of helium and neon isotopes in gas samples given to three significant figures. Values given in cm^3 per cm^3 of gas. Error is 1 sigma. Average values and the standard deviation are also provided.

Sample	^{36}Ar	Err	^{38}Ar	Err	^{40}Ar	Err	$^{40}Ar^{*}$	Err
Kidd Mine (2.4 km)								
12287	2.22E-07	0.02E-07	4.32E-08	0.06E-08	3.63E-03	0.03E-03	3.56E-03	0.05E-03
12299	3.23E-07	0.03E-07	6.25E-08	0.08E-08	4.46E-03	0.04E-03	4.36E-03	0.05E-03
Average	**2.73E-07**	**0.71E-07**	**5.28E-08**	**1.36E-08**	**4.04E-03**	**0.59E-03**	**3.96E-03**	**0.57E-03**
Kidd Mine (2.9 km)								
13684	2.65E-08	0.05E-08	5.96E-09	0.17E-09	2.05E-03	0.02E-03	2.05E-03	0.04E-03
13684	2.28E-08	0.05E-08	4.54E-09	0.22E-09	2.07E-03	0.02E-03	2.07E-03	0.05E-03
BH2	2.66E-08	0.07E-08	6.08E-09	0.25E-09	3.08E-03	0.03E-03	3.07E-03	0.08E-03
BH2	3.07E-08	0.13E-08	5.61E-09	0.43E-09	3.85E-03	0.03E-03	3.84E-03	0.17E-03
Average	**2.67E-08**	**0.32E-08**	**5.55E-09**	**0.70E-09**	**2.76E-03**	**0.87E-03**	**2.76E-03**	**0.87E-03**
Sudbury Mine 1 (1.7 km)								
170128	4.89E-06	0.05E-06	9.35E-07	0.09E-07	2.12E-02	0.02E-02	1.97E-02	0.03E-03
170128	4.12E-06	0.04E-06	8.05E-07	0.07E-07	1.82E-02	0.02E-02	1.70E-02	0.02E-03
170128	6.92E-06	0.07E-06	1.33E-06	0.01E-06	2.98E-02	0.03E-02	2.77E-02	0.04E-03
Average	**5.31E-06**	**1.45E-06**	**1.02E-06**	**0.27E-06**	**2.31E-02**	**0.60E-02**	**2.15E-02**	**0.56E-02**
Sudbury Mine 2 (1.4 km)								
47774	3.72E-06	0.04E-06	7.34E-07	0.09E-07	6.55E-02	0.06E-02	6.44E-02	0.08E-02
Average	**3.72E-06**	**0.04E-06**	**7.34E-07**	**0.09E-07**	**6.55E-02**	**0.06E-02**	**6.44E-02**	**0.08E-02**

Table A2. Concentrations of argon isotopes in gas samples given to three significant figures. Values given in cm^3 per cm^3 of gas. Error is 1 sigma. Average values and the standard deviation are also provided.

Sample	^{78}Kr	Err	^{80}Kr	Err	^{82}Kr	Err	^{83}Kr	Err	^{84}Kr	Err	^{86}Kr	Err
Kidd Mine (2.4 km)												
12287	3.64E-11	0.04E-11	2.29E-10	0.03E-10	1.17E-09	0.01E-09	1.17E-09	0.01E-09	5.79E-09	0.07E-09	1.78E-09	0.02E-09
12299	5.77E-11	0.07E-11	3.56E-10	0.04E-10	1.82E-09	0.02E-09	1.81E-09	0.02E-09	9.00E-09	0.11E-09	2.74E-09	0.03E-09
Average	**4.7E-11**	**1.51E-11**	**2.93E-10**	**0.90E-10**	**1.50E-09**	**0.46E-09**	**1.49E-09**	**0.46E-09**	**7.40E-09**	**2.27E-09**	**2.26E-09**	**0.68E-09**
Kidd Mine (2.9 km)												
13684	4.50E-12	0.06E-12	2.81E-11	0.03E-11	1.43E-10	0.02E-10	1.43E-10	0.02E-10	7.09E-10	0.08E-10	2.27E-10	0.02E-10
13684	5.10E-12	0.07E-12	3.18E-11	0.04E-11	1.61E-10	0.02E-10	1.61E-10	0.02E-10	7.99E-10	0.10E-10	2.48E-10	0.03E-10
BH2	5.57E-12	0.08E-12	3.49E-11	0.05E-11	1.76E-10	0.03E-10	1.77E-10	0.03E-10	8.76E-10	0.11E-10	2.83E-10	0.04E-10
BH2	5.93E-12	0.08E-12	3.70E-11	0.05E-11	1.87E-10	0.03E-10	1.87E-10	0.03E-10	9.26E-10	0.11E-10	2.97E-10	0.04E-10
Average	**5.28E-12**	**0.62E-12**	**3.29E-11**	**0.39E-11**	**1.67E-10**	**0.19E-10**	**1.67E-10**	**0.19E-10**	**8.28E-10**	**0.95E-10**	**2.64E-10**	**0.32E-10**
Sudbury Mine 1 (1.7 km)												
170128	8.82E-10	0.12E-10	5.57E-09	0.07E-09	2.85E-08	0.04E-08	2.84E-08	0.04E-08	1.41E-07	0.02E-07	4.33E-08	0.06E-08
170128	7.81E-10	0.10E-10	4.97E-09	0.06E-09	2.54E-08	0.03E-08	2.53E-08	0.03E-08	1.26E-07	0.02E-07	3.86E-08	0.05E-08
170128	1.33E-09	0.02E-09	8.47E-09	0.11E-09	4.33E-08	0.06E-08	4.32E-08	0.06E-08	2.15E-07	0.02E-07	6.59E-08	0.09E-08
Average	**9.97E-10**	**2.91E-10**	**6.34E-09**	**1.87E-09**	**3.24E-08**	**0.96E-08**	**3.23E-08**	**0.95E-08**	**1.61E-07**	**0.48E-07**	**4.93E-08**	**1.46E-08**
Sudbury Mine 2 (1.4 km)												
47774	6.94E-10	0.09E-10	4.38E-09	0.05E-09	2.23E-08	0.03E-08	2.23E-08	0.02E-08	1.11E-07	0.01E-07	3.41E-08	0.04E-08
Average	**6.94E-10**	**0.09E-10**	**4.38E-09**	**0.05E-09**	**2.23E-08**	**0.03E-08**	**2.23E-08**	**0.02E-08**	**1.11E-07**	**0.01E-07**	**3.41E-08**	**0.04E-08**

Table A3. Concentrations of krypton isotopes in gas samples given to three significant figures. Values given in cm^3 per cm^3 of gas. Error is 1 sigma. Average values and the standard deviation are also provided.

Sample	^{124}Xe	Err	^{126}Xe	Err	^{128}Xe	Err	^{129}Xe	Err	^{130}Xe	Err
Kidd Mine (2.4 km)										
12287	1.53E-12	0.03E-12	1.41E-12	0.02E-12	3.09E-11	0.05E-11	4.24E-10	0.07E-10	6.46E-11	0.10E-11
12299	2.10E-12	0.04E-12	1.93E-12	0.04E-12	4.19E-11	0.07E-11	5.85E-10	0.10E-10	8.85E-11	0.14E-11
Average	**1.81E-12**	**0.40E-12**	**1.67E-12**	**0.37E-12**	**3.64E-11**	**0.78E-11**	**5.04E-10**	**1.14E-10**	**7.66E-11**	**1.69E-11**
Kidd Mine (2.9 km)										
13684	1.96E-13	0.03-E13	1.79E-13	0.03E-13	3.94E-12	0.06E-12	5.49E-11	0.08E-11	8.17E-12	0.12E-12
13684	2.17E-13	0.03E-13	2.00E-13	0.03E-13	4.34E-12	0.06E-12	6.10E-11	0.09E-11	9.09E-12	0.13E-12
BH2	2.67E-13	0.04E-13	2.46E-13	0.04E-13	5.36E-12	0.08E-12	7.51E-11	0.11E-11	1.11E-11	0.02E-11
BH2	2.83E-13	0.04E-13	2.62E-13	0.04E-13	5.66E-12	0.08E-12	7.92E-11	0.12E-11	1.17E-11	0.02E-11
Average	**2.41E-13**	**0.41E-13**	**2.22E-13**	**0.39E-13**	**4.83E-12**	**0.82E-12**	**6.76E-11**	**1.14E-11**	**1.00E-11**	**0.17-11**
Sudbury Mine 1 (1.7 km)										
170128	2.60E-11	0.04E-11	2.40E-11	0.04E-11	5.19E-10	0.08E-10	7.13E-09	0.11E-09	1.09E-09	0.02E-09
170128	2.41E-11	0.04E-11	2.23E-11	0.04E-11	4.82E-10	0.08E-10	6.63E-09	0.10E-09	1.02E-09	0.02E-09
170128	4.11E-11	0.07E-11	3.86E-11	0.07E-11	8.31E-10	0.14E-10	1.14E-08	0.02E-08	1.75E-09	0.03E-09
Average	**3.04E-11**	**0.93E-11**	**2.83E-11**	**0.90E-11**	**6.11E-10**	**1.92E-10**	**8.38E-09**	**2.61E-09**	**1.29E-09**	**0.40E-09**
Sudbury Mine 2 (1.4 km)										
47774	2.37E-11	0.04E-11	2.24E-11	0.04E-11	4.83E-10	0.08E-10	6.63E-09	0.11E-09	1.01E-09	0.02E-09
Average	**2.37E-11**	**0.04E-11**	**2.24E-11**	**0.04E-11**	**4.83E-10**	**0.08E-10**	**6.63E-09**	**0.11E-09**	**1.01E-09**	**0.02E-09**

Table A4. Concentrations of light xenon isotopes in gas samples given to three significant figures. Values given in cm^3 per cm^3 of gas. Error is 1 sigma. Average values and the standard deviation are also provided.

Sample	^{131}Xe	Err	^{132}Xe	Err	^{134}Xe	Err	^{136}Xe	Err	^{136}Xe*	Err
Kidd Mine (2.4 km)										
12287	6.46E-11	0.10E-11	3.37E-10	0.05E-10	4.34E-10	0.06E-10	1.79E-10	0.03E-10	1.56E-10	0.03E-10
12299	8.85E-11	0.14E-11	4.82E-10	0.08E-10	6.00E-10	0.09E-10	2.48E-10	0.04E-10	2.16E-10	0.04E-10
Average	**7.66E-11**	**1.69E-11**	**4.10E-10**	**1.03E-10**	**5.17E-10**	**1.17E-10**	**2.14E-10**	**0.49E-10**	**1.86E-10**	**0.43E-10**
Kidd Mine (2.9 km)										
13684	8.17E-12	0.12E-12	4.36E-11	0.06E-11	6.22E-11	0.09E-11	3.40E-11	0.05E-11	3.36E-11	0.05E-11
13684	9.09E-12	0.13E-12	5.39E-11	0.08E-11	6.83E-11	0.10E-11	3.67E-11	0.05E-11	3.58E-11	0.05E-11
BH2	1.11E-11	0.02E-11	5.91E-11	0.09E-11	8.47E-11	0.12E-11	4.69E-11	0.07E-11	4.65E-11	0.07E-11
BH2	1.17E-11	0.02E-11	6.23E-11	0.09E-11	8.83E-11	0.13E-11	4.80E-11	0.07E-11	4.70E-11	0.07E-11
Average	**1.00E-11**	**0.17E-11**	**5.47E-11**	**0.82E-11**	**7.59E-11**	**1.26E-11**	**4.14E-11**	**0.71E-11**	**4.07E-11**	**0.70E-11**
Sudbury Mine 1 (1.7 km)										
170128	1.09E-09	0.02E-09	5.71E-09	0.09E-09	7.35E-09	0.11E-09	3.01E-09	0.05E-09	2.61E-09	0.04E-09
170128	1.02E-09	0.02E-09	5.31E-09	0.08E-09	6.85E-09	0.10E-09	2.80E-09	0.04E-09	2.43E-09	0.04E-09
170128	1.75E-09	0.03E-09	9.11E-09	0.15E-09	1.17E-08	0.02E-08	4.79E-09	0.08E-09	4.15E-09	0.07E-09
Average	**1.29E-09**	**0.40E-09**	**6.71E-09**	**2.09E-09**	**8.64E-09**	**2.68E-09**	**3.53E-09**	**1.09E-09**	**3.07E-09**	**0.94E-09**
Sudbury Mine 2 (1.4 km)										
47774	1.01E-09	0.02E-09	5.34E-09	0.09E-09	7.17E-09	0.11E-09	3.31E-09	5.49E-11	3.04E-09	0.05E-09
Average	**1.01E-09**	**0.02E-09**	**5.34E-09**	**0.09E-09**	**7.17E-09**	**0.11E-09**	**3.31E-09**	**5.49E-11**	**3.04E-09**	**0.05E-09**

Table A5. Concentrations of heavy xenon isotopes in gas samples given to three significant figures. Values given in cm^3 per cm^3 of gas. Error is 1 sigma. Average values and the standard deviation are also provided.

Sample	$^{78}Kr/^{82}Kr$	Err	$^{82}Kr/^{82}Kr$	Err	$^{83}Kr/^{82}Kr$	Err	$^{84}Kr/^{82}Kr$	Err	$^{86}Kr/^{82}Kr$	Err
Kidd Mine (2.4 km)										
12287	1.587E-01	0.002	5.10	0.01	5.08	0.01	25.28	0.04	7.76	0.01
12299	1.615E-01	0.004	5.10	0.01	5.07	0.01	25.21	0.04	7.69	0.01
Average	**1.60E-01**	**0.02**	**5.098**	**0.003**	**5.08**	**0.01**	**25.2**	**0.1**	**7.72**	**0.05**
Kidd Mine (2.9 km)										
13684	1.61E-01	0.01	5.13	0.01	5.11	0.01	25.4	0.1	8.10	0.02
13684	1.61E-01	0.01	5.13	0.02	5.09	0.01	25.3	0.1	7.84	0.02
BH2	1.61E-01	0.01	5.17	0.03	5.12	0.03	25.4	0.1	8.21	0.04
BH2	1.62E-01	0.01	5.16	0.02	5.10	0.02	25.3	0.1	8.12	0.03
Average	**1.616E-01**	**0.004**	**5.15**	**0.02**	**5.11**	**0.01**	**25.3**	**0.1**	**8.05**	**0.16**
Sudbury Mine 1 (1.7 km)										
170128	1.579E-01	0.002	5.09	0.01	5.09	0.01	25.30	0.03	7.76	0.01
170128	1.571E-01	0.002	5.10	0.01	5.09	0.01	25.31	0.02	7.76	0.01
170128	1.564E-01	0.002	5.10	0.01	5.088	0.005	25.30	0.02	7.76	0.01
Average	**1.57E-01**	**0.01**	**5.095**	**0.002**	**5.089**	**0.001**	**25.304**	**0.002**	**7.759**	**0.002**
Sudbury Mine 2 (1.4 km)										
47774	1.585E-01	0.003	5.11	0.01	5.09	0.01	25.31	0.04	7.79	0.01
Average	**1.585E-01**	**0.003**	**5.11**	**0.01**	**5.09**	**0.01**	**25.31**	**0.04**	**7.79**	**0.01**

Table A6. Isotopic ratios within samples for krypton given to three significant figures. Where the uncertainty is lower than the third significant figure an additional significant figure is given. Error represents 1 sigma. Average values and the standard deviation are also provided.

Appendix C1: Determination of Rayleigh Fractionation for Kidd Creek Mine 2.9 km samples

To determine whether Rayleigh fractionation can satisfactorily explain the elemental ratios observed (Figure 2, Main text) an error-weighted Chi-squared (χ^2) approach was applied (Ballentine and Hall, 1999). This technique allows statistical assessment of the goodness of fit of a model with observed isotopic ratios. Here two models are explored; 1. Open (Rayleigh) degassing and 2. Closed (batch) degassing. The starting noble gas composition for both models was taken as seawater at 10 °C (Kipfer et al., 2002) and was modelled as discrete steps of 1 cm^3 of gas exsolving from 10,000 cm^3 of water. In the open model this gas is lost from the system and in the closed model the gas is retained in the gas phase. Fit is assessed by comparing the modelled noble gas ratios in the gas phase to measured ratios. By varying the temperature, salinity and degree of degassing it was possible to derive the best fit (minimised χ^2) between the observed and modelled values. With three isotopic ratios to compare to the model ($^{20}Ne/^{36}Ar$, $^{84}Kr/^{36}Ar$ and $^{130}Xe/^{36}Ar$) this scenario has 2 degrees of freedom. As additional constraints, the viable salinity range of the degassing fracture fluid was set between 2.7 - 4.5 moles/litre and temperature between 20-50 °C. These were based on the local geothermal gradient of 10-15 °C/km (Grasby et al., 2012) and supported by fluid observations in Kidd Creek Mine at 2.4 and 2.9 km.

Using this approach a χ^2 was generated for both open and closed degassing models which fit within 2 σ ($\chi^2 = 6.18$) of the model over a thermal range of 24-50 & 18-50 °C at all salinities.

The best fit for both scenarios (χ^2 = 4.2 and 4.1 respectively) occurred at 50 °C and 4.5 moles/litre salinity. These open and closed degassing models indicate a relative ^{36}Ar loss of

17% and 39% respectively from the water phase. Although a better fit could be achieved if the present-day temperature/salinity ranges were increased in the model there is no physical justification for this. This elemental fractionation is considered most likely due to Rayleigh degassing, given the open nature of the boreholes allowing unrestricted gas loss from the system over time. However, either gas loss process can explain measured isotopic deviation from the chosen initial composition.

To derive initial concentrations for Kidd Creek Mine 2.9 km prior to degassing the relative enrichment/depletion factor over ASW values is determined using ^{20}Ne, ^{36}Ar, ^{84}Kr and ^{130}Xe concentrations for each noble gas and all other isotopes are adjusted accordingly. Typically, no isotopic fractionation occurs during degassing, although the different Henry's Law constants results in significant elemental fractionation (Ballentine et al., 2002). In the case of helium, which has a similar solubility to that of neon (Crovetto et al., 1982; Smith and Kennedy, 1983; Smith, 1985), the degassing factor estimated for neon is applied.

Appendix C2: Determination of early atmospheric $^{131\text{-}136}$Xe component

According to the atmospheric xenon evolution model (Pujol et al., 2009), wherever a $^{124\text{-}128}$Xe xenon excess is observed, a corresponding deficit in the heavy isotopes should also be present (Pujol et al., 2011; Avice and Marty, 2014). However, due to a significant uranium-derived radiogenic component, this cannot be directly observed in these samples. We can statistically test whether a fractionated $^{131\text{-}136}$Xe component is consistent with the results by determining whether the observed $^{131\text{-}136}$Xe/^{130}Xe within the system can produced via mixing of fractionated atmospheric and a uranogenic xenon end member.

By varying the relative contributions of each end-member from 0-100 % at 0.1 % intervals, the isotopic evolution of the mixture can be modelled and compared with the experimental data. This approach is done for both an early, fractionated atmosphere, and for modern unfractionated air. For the initial early atmospheric component, the average $^{124\text{-}128}$Xe per mil isotopic fractionation for each locality was used to derive a corresponding isotopic deficit for the $^{131\text{-}136}$Xe/^{130}Xe ratios. The standard deviation in the measured $^{124\text{-}128}$Xe fractionation was used to define the upper and lower fractionation limits. These are given in Table A3.1.

Location	Ave $^{124\text{-}128}$Xe fractionation (‰)	Uncertainty (‰)
Kidd Mine (2.4 km, 2013)	3.3	0.8
Kidd Mine (2.4 km, this work)	2.6	2.6
Kidd Mine (2.9 km)	6.7	4.0
Sudbury Mine 1 (1.7 km)	2.5	1.1
Sudbury Mine 2 (1.4 km)	3.0	2.7

Table A3.1. Average per mil fractionation of $^{124\text{-}128}$Xe per amu. All values calculated as per Figure 5 caption (main text). Uncertainty is the standard deviation of all calculated individual excesses per amu and represents 1 σ.

This model was applied to the Kidd Creek mine 2.9 km and Mine 1 Datasets. Neither Mine 2 nor the new Kidd Creek Mine 2.4 km were modelled as only one data point was available for Mine 1 while the resampled 2.4 km fluids reveal ongoing isotopic evolution towards less ancient fluids and therefore may not be representative of a 2-component mixing. Consequently, the Chi-squared analysis was not performed for either locality.

With 4 isotopic ratios (3 degrees of freedom) the 2 σ χ^2 critical value is defined as 8.02. The lowest χ^2 value represents the best fit between modelled and measured conditions for the model parameters. The results are given in Table A3.2.

Sample	Lowest χ^2 value	Uranogenic

		contribution (%)
Kidd Mine		
(2.4 km, 2013)		
Modern Air	2.7	4.9 - 6.5
Ancient air (low)	0.7	5.4 - 7.3
Ancient air (mid)	0.6	5.7 - 7.5
Ancient air (high)	0.8	5.9 - 7.7
Kidd Mine		
(2.9 km)		
Modern Air	2.8	19.2 - 21.8
Ancient air (low)	2.3	19.7 - 22.4
Ancient air (mid)	1.6	20.3 - 23.2
Ancient air (high)	1.0	21.0 - 24.0
Sudbury Mine 1 (1.7 km)		
Modern Air	2.6	2.7 - 3.2
Ancient air (low)	1.0	3.0 - 3.5
Ancient air (mid)	0.6	3.2 - 3.7
Ancient air (high)	0.7	3.4 - 3.9

Table A3.2. Results from χ^2 analysis for two end-member mixing between uranogenic $^{131-136}$Xe and a modern, and for ancient air components. The ancient air component was derived using the positive deviation observed for $^{124-128}$Xe with mid, low and high representing the mean and upper and lower standard deviation respectively. Uranogenic contribution and lowest χ^2 value are reported for the original Kidd Mine study, the new 2.9 km data and for Sudbury Mine 1. The range of uranium contribution was calculated using the 2 σ χ^2 value.

In all systems, a χ^2 minima is identified below the 2 σ critical value for both binary mixing models. This indicates the model resolution lacks the detail to categorically discern between the two mixing scenarios. Therefore, although statistically a modern air end member cannot be ruled out, an early fractionated atmospheric component remains viable which is consistent with the shielded xenon isotopes and the fractionation model initially proposed by Pujol et al. (2011).

These models support the overall multiple lines of evidence presented here that demonstrate that there is a much greater $^{131-136}$Xe radiogenic component present in the fracture fluids at 2.9 km at Kidd Creek Mine, compared to the 2013 2.4 km samples (A 20-24 % uranogenic

$^{131\text{-}136}$Xe contribution to the measured $^{131\text{-}136}$Xe of compared with 5-8 %). In Sudbury Mine 1 a smaller radiogenic component of 3-4 % is present. In all cases, the degree of radiogenic contribution calculated using this technique is consistent with the xenon-derived ages which supports the validity of this model.

Appendix B: Analysis of fluids for ^{18}O and ^{2}H

B1 Introduction

This procedure was used to analyze fluid samples for their ^{18}O and ^{2}H content at the University of Waterloo using the MP-GVI-IsoPrime and EA/HT-Micromass-IsoPrime systems respectively. Oxygen (^{18}O) is determined by CO_2 equilibration using standard procedures based on the principles of Epstein and Mayeda (1953). Deuterium (^{2}H) determinations are performed on hydrogen gas produced from water reduced on hot chromium as per Morrison et al. (2001). Accuracy of analysis for both techniques is confirmed by analysing duplicates and comparison to international reference standards sourced from the IAEA. The analytical methodologies are now outlined:

B2 ^{18}O sample analysis

All samples were analysed using the MP-GVI-IsoPrime instrument. First 200 µL aliquots of water samples are pipetted into septum vials and flushed with a 2 % CO_2-helium mixture. Next samples are placed into an aluminum tray maintained at 40 $^{\circ}C$ for a minimum of 3.5 hours to allow oxygen isotopic equilibration between the CO_2 and H_2O. Following this the CO_2 is extracted automatically with a Gilson Autosampler connected to a GVI Multiprep automated sample preparation system which uses a 500 µl sample column to separate CO_2, N_2, O_2 and H_2O. The purified CO_2 is then transported via helium carrier gas to the IsoPrime continuous flow isotope ratio mass spectrometer system (CF-IRMS) where isotope ratios are measured to a precision of ± 0.2 ‰.

22

23 **B3 ^{18}O Quality Assurance/Quality Control**

24 Quality control is maintained by analysing working laboratory water standards at the beginning
25 middle and end of each 60-sample batch. These working standards are water kept in stock bottles
26 and calibrated to the international reference materials VSMOW (Vienna Standard Mean Ocean
27 Water) and VSLAP (Vienna Standard Light Antarctic Precipitation) from the International
28 Atomic Energy Agency (IAEA). All results therefore are verified and recorded based on standard
29 corrections performed based on the calculated laboratory/VSMOW/VSLAP calibration. Values
30 were additionally verified by analysing duplicates approximately every tenth sample.

31

32 **B4 ^{2}H sample analysis**

33 All samples were analysed using the EA/HT-Micromass-IsoPrime mass spectrometer. Initially
34 the cconductivity of groundwater samples was measured. Where conductivity is high (> 0.1
35 S/m) samples were treated accordingly by azeotropic distillation to prevent hydrogen isotopic
36 fractionation (Horita and Gat, 1988). All samples were then pipetted into 2-ml septum vials
37 which were then are placed into a CTC AS200 Auto-sampler (LAS), capable of holding up to
38 110 samples, standards and repeats. To avoid contamination, the auto-ampler syringe is pre-
39 rinsed twice with new sample, after which 0.2 μL of water was sampled. This water was then
40 injected into a heated inlet system where a helium gas stream carries it to a Eurovector Euro
41 3000 Elemental Analyzer with a 960 °C furnace packed with chromium. Through reaction with
42 the chromium the water was reduced to hydrogen gas, which was then carried via helium stream

to the Micromass IsoPrime mass spectrometer which determined the δ^2H value for the sample. The precision for this technique is ± 0.8 ‰.

B5 ^2H Quality Assurance/Quality Control

Sample values are determined based on standard corrections using calibrated working analytical standards coupled with the international reference materials VSMOW (Vienna Standard Mean Ocean Water) and VSLAP (Vienna Standard Light Antarctic Precipitation) from the International Atomic Energy Agency (IAEA). All sample values were verified by duplicate analysis.

B6 Additional References

Epstein, S. and Mayeda, T. 1953. Variation of O-18 Content of Waters from Natural Sources. *Geochimica Et Cosmochimica Acta* 4, 213-224.

Horita, J. and Gat, J.R. 1988. Procedure for the Hydrogen Isotope Analysis of Water from Concentrated Brines. *Chemical Geology* 72, 85-88.

Morrison, J. Brockwell, T. Merren, T. Fourel, F. and Phillips, A.M. 2001. On-line high-precision stable hydrogen isotopic analyses on nanoliter water samples. *Analytical Chemistry* 73, 3570-3575.